Check for updates

DOI: 10.1002/mrm.30607

RESEARCH ARTICLE

Multidimensional RF pulse design using auto-differentiable spin-domain optimization and its application to reduced field-of-view imaging

Jiayao Yang¹ | Jon-Fredrik Nielsen^{1,2,3} | Jeffrey A. Fessler^{1,2,3} | Yun Jiang^{2,3}

Correspondence

Yun Jiang, Department of Radiology, University of Michigan, Med Sci I, Room 3217, 1301 Catherine St., Ann Arbor, MI 48108, USA.

Email: yunjiang@umich.edu

Funding information

National Institutes of Health. Grant/Award Numbers: R01CA284172. R01EB032378, R37CA263583; Siemens Healthineers

Abstract

Purpose: Develop a general radiofrequency (RF) pulse design algorithm for the design of three-dimensional (3D) spatially selective refocusing pulses and explore their potential applications in reduced field-of-view imaging.

Methods: Spin-domain representation was used to describe the effect of RF pulses and to formulate the optimization problem. The implementation was based on an auto-differentiable simulator. Spatially selective excitation and refocusing pulses for a small regions of interest were designed with consideration of hardware limits and B₀ and B₁⁺ inhomogeneities. The designed RF pulses were validated in simulation as well as in vivo experiments in brain and prostate on a 3T scanner.

Results: Pulses of short duration (4.15 ms) were designed for 3D tailored excitation and refocusing accounting for B₀ and B₁⁺ inhomogeneities. The computation time for each design was approximately 7 min. Improved outer-volume signal suppression in phantom and in vivo spin-echo imaging experiments was achieved by combining 3D excitation and refocusing pulses compared with using only one 3D pulse. The potential of using tailored 3D pulses to obtain images with higher spatial resolution $(1 \times 1 \times 3 \text{ mm}^3)$ and less distortion with the same scan time was demonstrated by acquiring reduced field-of-view 3D images of brain and prostate.

Conclusion: The proposed algorithm jointly optimizes the RF and gradient waveforms given an initial pulse and a desired spin-domain target pattern. Our approach is broadly applicable to the design of excitation and refocusing pulses and complements existing methods based on describing individual spin isochromatic behavior. Combining 3D excitation and 3D refocusing pulses produced better spatial selectivity than using a combination of one-dimensional and 3D pulses.

KEYWORDS

auto-differentiable, constrained optimization, multidimensional RF pulse design, reduced field of view, spin domain

This is an open access article under the terms of the Creative Commons Attribution-NonCommercial License, which permits use, distribution and reproduction in any medium, provided the original work is properly cited and is not used for commercial purposes.

¹Department of Electrical Engineering and Computer Science, University of Michigan, Ann Arbor, Michigan, USA

²Department of Biomedical Engineering, University of Michigan, Ann Arbor, Michigan, USA

³Department of Radiology, University of Michigan, Ann Arbor, Michigan, USA

1 | INTRODUCTION

MRI is a noninvasive medical imaging technology that provides detailed images of soft tissue for diagnosing diseases. It uses radiofrequency (RF) and gradient magnetic fields to manipulate the magnetization of protons to generate images of the human body. Typically, one-dimensional (1D) RF pulses are used to selectively excite a slice or a slab, and the field of view (FOV) is set to encompass the entire object to avoid aliasing. However, imaging with such a "full" FOV can be inefficient when the region of interest (ROI) is smaller than the FOV. In comparison, reduced FOV imaging, 1-3 achieved by either exciting the ROI, 6 or suppressing the signal outside the ROI, 6 has the potential to reduce scan time, 7 improve spatial resolution, or minimize the geometric distortion caused by a prolonged readout.

One method for achieving reduced FOV imaging is the use of multidimensional RF pulses, which applies RF and gradient fields in multiple directions to achieve spatial selectivity. However, designing these multidimensional RF pulses is challenging because it requires optimization of both RF and gradient waveforms. This optimization problem is generally nonconvex due to the nonlinearity of spin physics. Additionally, factors such as pulse duration,⁸ RF power deposition,⁹ and B₀ and B₁⁺ inhomogeneities^{10,11} must also be considered alongside spatial selectivity.

Numerous methods have been proposed for designing multidimensional RF pulses. Most of these methods rely on the small-tip approximation, which assumes a linear relationship between the applied RF pulse and the resulting magnetization. Some algorithms optimize both gradient and RF waveforms, whereas others focus on optimizing the RF waveform using a predefined gradient trajectory, using this approximation. However, this approximation may not hold for large flip angles.

When designing large flip-angle pulses, more complex modeling of the Bloch equations is required. One approach involves using optimal control theory, ^{21–24} which seeks to find the RF field as a control input to manipulate spins based on the Bloch equation. Another method uses an automatically differentiable Bloch equation simulator ^{25–28} to provide a precise gradient of the loss function for efficient and accurate optimization. However, design methods based on Bloch equation simulation are primarily suitable for cases in which the initial and final spin isochromatic magnetization can be specified, such as in the design of excitation, saturation, or inversion pulses. In these

pulses, the initial magnetization (M_0) is at equilibrium $(M_0 = [0\ 0\ 1]^T)$, and the final (and target) magnetization, following the application of the RF pulse, is represented as a set of length-3 spin (isochromat) magnetization vectors positioned at specific locations within the imaging volume. However, for refocusing pulses, where the initial and final spin isochromat magnetization vectors are unknown, specifying multiple initial conditions and their corresponding final states is necessary.²² Therefore, using the spin-domain representation²⁹ for designing refocusing pulses may be more straightforward than working with the magnetization vectors in the Bloch equation simulator.

In this work, we introduce a novel spin-domain algorithm for the joint design of RF and gradient waveforms for multidimensional pulse design that does not require explicit descriptions of the initial and final isochromatic magnetization. The spin-domain representation forms the basis of the Shinnar-Le Roux (SLR) algorithm,²⁹ which is an effective approach for designing RF pulses with large flip angles. However, extending the SLR algorithm to the design of multidimensional RF pulses is complex and computationally demanding.³⁰ Other techniques using the SLR algorithm^{31,32} or a spin-domain representation^{23,33–35} have been proposed for designing multidimensional refocusing pulses. However, these methods used predefined gradients to simplify the design process, which may lead to suboptimal performance, because the gradient waveforms are not optimized based on the ROI.

A recent study used an auto-differentiable Bloch equation simulator to design saturation and inversion pulses.²⁶ Inspired by this approach, we propose using an auto-differentiable simulator of spin-domain parameters, with explicitly derived Jacobians to reduce the computation time, for designing RF pulses with large flip angles. Our RF design algorithm accounts for systematic imperfections, such as B₀ and B₁⁺ inhomogeneities, and hardware limitations, such as peak RF power, maximum gradient strength, and maximum gradient slew rate, by solving a constrained optimization problem. Although initially developed for designing refocusing pulses, our algorithm can also be adapted for excitation pulse design. In this study, our algorithm designed three-dimensional (3D) excitation and refocusing pulses with a duration of 4.15 ms and a maximum B_1 of 10 μT for a 3D cubic region with varying sizes. We evaluated the performance of these multidimensional RF pulses using numerical simulations and experiments using a phantom and healthy subjects on a 3T MRI scanner.

2.1 | Spin-domain representation

The rotation of magnetization induced by an RF pulse can be expressed using the spin-domain parameters α and β as follows:

$$\begin{bmatrix} M_{xy}^{+} \\ M_{xy}^{+*} \\ M_{z}^{+} \end{bmatrix} = \begin{bmatrix} (\alpha^{*})^{2} & -\beta^{2} & 2\alpha^{*}\beta \\ -(\beta^{*})^{2} & \alpha^{2} & 2\alpha\beta^{*} \\ -\alpha^{*}\beta^{*} & -\alpha\beta & \alpha\alpha^{*} - \beta\beta^{*} \end{bmatrix} \begin{bmatrix} M_{xy}^{-} \\ M_{xy}^{-*} \\ M_{z}^{-} \end{bmatrix}$$
(1)

where $M_{xy}^- = M_x^- + iM_y^-$ is the initial transverse magnetization; M_z^- is the initial longitudinal magnetization; and M_{xy}^+ and M_z^+ are the transverse magnetization and longitudinal magnetization after applying the RF pulse. The parameters α and β , known as Cayley-Klein parameters, ²⁹ spinors, or SU2 representation, are two complex-valued parameters defined as follows:

$$\alpha = \cos \phi / 2 - i n_z \sin \phi / 2$$

$$\beta = -i (n_x + i n_y) \sin \phi / 2$$
 (2)

where $\mathbf{n} = (n_x, n_y, n_z)^T$ is the rotation axis with unit norm $\|\mathbf{n}\| = 1$, and α and β satisfy the condition $|\alpha|^2 + |\beta|^2 = 1$. Here, ϕ is the rotation angle produced by the RF pulse.

2.2 | Spin-domain representation for refocusing pulses

The rotation of magnetization by 180° in the transverse plane along the x-axis, caused by a refocusing pulse, can be expressed as $M_{xy}^+ = M_{xy}^{-*}$. By comparing this expression with Eq. (1), we obtain

$$\alpha = 0, \beta^2 = -1. \tag{3}$$

If this 180° rotation is applied around an axis $n = (\cos \psi, \sin \psi, 0)^T$ in the transverse plane, the effect of the rotation can be further expressed as $M_{xy}^+ = M_{xy}^{-*} e^{i2\psi}$, leading to $\alpha = 0$ and $\beta^2 = -e^{i2\psi}$ when compared with Eq. (1).

For magnetization outside the refocusing region, the magnetization after the pulse is given by

$$M_{xy}^{+} = (\alpha^{*})^{2} M_{xy}^{-} - \beta^{2} M_{xy}^{-*}. \tag{4}$$

As discussed in Pauly et al.,²⁹ the first term in Eq. (4) integrates to zero when a pair of crusher gradients surrounds the refocusing pulse, resulting in $M_{xy}^+ = -\beta^2 M_{xy}^{-*}$. For regions not intended to be refocused, β can be set to zero. Therefore, the spin-domain representation

simplifies the design of refocusing pulse by focusing on the β^2 pattern of the RF pulse. This approach avoids the need for explicitly describing the orientation of spin isochromat magnetization vectors, which is required in design algorithms that directly integrate the Bloch equation.

2.3 | Spin-domain representation for excitation pulses

For an excitation pulse, the transverse and longitudinal magnetization after the pulse are given by $M_{xy}^+ = 2\alpha^*\beta M_0$ and $M_z^+ = (\alpha\alpha^* - \beta\beta^*)M_0$, respectively, with initial magnetization $M_{xy}^- = [0\ 0\ M_0]^T$. For an excitation pulse with flip angle θ applied along an axis $\mathbf{n} = (\cos\psi, \sin\psi, 0)^T$ in the transverse plane, the resulting transverse and longitudinal magnetization are $M_{xy}^+ = i\sin\theta\ M_0e^{i\psi}$ and $M_z^+ = \cos\theta\ M_0$. Compared with the results from spin-domain representations, we obtain

$$2\alpha^*\beta = ie^{i\psi}\sin\theta,$$

$$\alpha\alpha^* - \beta\beta^* = \cos\theta.$$
 (5)

From the relationship between α and β , we can derive the magnitudes of α and β as follows:

$$|\alpha| = \sqrt{\frac{1 + \cos \theta}{2}},$$

$$|\beta| = \sqrt{\frac{1 - \cos \theta}{2}}.$$
(6)

These expressions describe how the parameters α and β relate to the desired flip angle θ for excitation pulses.

2.4 | RF pulse-design formulation

We express the design of multidimensional RF pulses as an optimization problem. Let N_t denote the number of time points used to represent a pulse and let m denote the total number of spins in the design. The complex RF waveform is represented by $\mathbf{b} \in \mathbb{R}^{2\times N_t}$ for its real and imaginary components, and the gradient waveform is represented by $\mathbf{g} \in \mathbb{R}^{3\times N_t}$. Given an RF waveform \mathbf{b} and gradient waveform \mathbf{g} , we simulate spin-domain rotation parameters at each spatial location. The design problem is generally expressed as follows:

$$\underset{\mathbf{b} \in \mathbb{R}^{2 \times N_t}, \mathbf{g} \in \mathbb{R}^{3 \times N_t}}{\arg\min} \mathcal{L} = f(\boldsymbol{\alpha}_T(\mathbf{b}, \mathbf{g}), \boldsymbol{\beta}_T(\mathbf{b}, \mathbf{g}), \boldsymbol{\alpha}_D, \boldsymbol{\beta}_D) + \mathcal{R}(\mathbf{b})$$

$$\begin{aligned} & \|\mathbf{b}_t\|_2 \leq b_{\max} \\ \text{subject to} & & \|\mathbf{g}_t\|_{\infty} \leq g_{\max} \\ & & & \|(\mathbf{D}\mathbf{g})_t\|_{\infty} \leq s_{\max} \end{aligned} \tag{7}$$

.5222594, 2025, 5, Downloaded from https://onlinelibrary.wiley.com/doi/10.1002/mrm.30607 by University Of Michigan Library, Wiley Online Library on [28/08/2025]. See the Terms ions) on Wiley Online Library for rules of use; OA articles are governed by the applicable Creative Commons where \mathcal{L} is the loss function; $\alpha_T \in \mathbb{C}^m, \beta_T \in \mathbb{C}^m$ are simulated spin-domain parameters at the end of the RF pulse and gradient (i.e., at time T) for m spins; $\alpha_{\rm D} \in \mathbb{C}^m, \beta_{\rm D} \in \mathbb{C}^m$ are the target values; f is a function representing the error between the simulated and target values; and $\mathcal{R}(\mathbf{b})$ is a regularization term for constraining the total RF energy. The terms $\mathbf{b}_t = [b_{real,t}, b_{imag,t}]^T, \mathbf{g}_t =$ $[g_{x,t}, g_{y,t}, g_{z,t}]^T$, $(\mathbf{D}\mathbf{g})_t = [(\mathbf{D}\mathbf{g})_{x,t}, (\mathbf{D}\mathbf{g})_{y,t}, (\mathbf{D}\mathbf{g})_{z,t}]^T$, resenting the RF amplitude, gradient amplitude, and gradient slew rate at time point t, are constrained by the peak RF amplitude (b_{max}), the maximum gradient strength (g_{max}) , and the maximum slew rate (s_{max}) , respectively. The matrix **D** is the time-difference operator that computes the slew rate from the gradient. The notation $\|\cdot\|_2$ is the vector ℓ_2 norm, which is used for constraints on the magnitude of the RF waveform, and $\|\cdot\|_{\infty}$ is the vector ℓ_{∞} norm, which is used for constraints independently applied to each channel of the gradients.

Specifically, we formulated the 3D refocusing pulse design problem with the following cost function:

$$\mathcal{L} = \sum_{i=1}^{m} w_i \left| \beta_{T,i}^2(\mathbf{b}, \mathbf{g}) - \beta_{D,i}^2 \right| + \lambda ||\mathbf{b}||_2^2$$
 (8)

where $\beta_{T,i}$ and $\beta_{D,i}$ denote the simulated and desired values for the magnetization at spatial location i; w_i is the weighting function at spatial location i; and λ is the regularization parameter for constraining the RF energy. The $|\cdot|$ computes the magnitude of the complex number, and the phase of desired $\beta_{D,i}^2$ within the ROI was chosen to be the same.

Similarly, we propose the following cost function for the 3D excitation pulse design problem:

$$\mathcal{L} = \sum_{i=1}^{m} w_i \{ \left| \alpha_{T,i}^*(\mathbf{b}, \mathbf{g}) \beta_{T,i}(\mathbf{b}, \mathbf{g}) - \frac{i}{2} e^{i\psi} \sin \theta_i \right|^2 + (\left| \beta_{T,i}(\mathbf{b}, \mathbf{g}) \right| - \left| \beta_{D,i} \right|)^2 \} + \lambda \|\mathbf{b}\|_2^2$$
(9)

where θ_i is the desired flip angle at spatial location i, and ψ is the phase of the RF pulse. The term $\left|\alpha_{T,i}^*\beta_{T,i} - \frac{i}{2}e^{i\psi}\sin\theta_i\right|$ minimizes the error of the transverse magnetization, whereas the term $\left|\beta_{T,i}(\mathbf{b},\mathbf{g})\right| - \left|\beta_{D,i}\right|$ focuses on the longitudinal magnetization, ensuring that the flip angle is uniquely defined from the spin-domain representations.

3 | METHODS

3.1 | Spin-domain simulation using explicit Jacobians

We computed the spin-domain rotation parameters using the hard-pulse approximation that assumes that both ${\bf b}$

and **g** are piece-wise constant functions with uniform sample spacing Δt . For simplicity, we ignored T_1 and T_2 relaxation. The evolution of the spin-domain rotation parameters over Δt is as follows:

$$\begin{bmatrix} \alpha_t \\ \beta_t \end{bmatrix} = \begin{bmatrix} a_t & -b_t^* \\ b_t & a_t^* \end{bmatrix} \begin{bmatrix} \alpha_{t-1} \\ \beta_{t-1} \end{bmatrix}$$

where a_t and b_t are calculated from Eq. (2) using the rotation produced by the effective magnetic field $\mathbf{B}_{\mathrm{eff},t}$. A rotation produced by $\mathbf{B}_{\mathrm{eff},t}$ is around the axis $\mathbf{n} = \frac{\mathbf{B}_{\mathrm{eff},t}}{\|\mathbf{B}_{\mathrm{eff},t}\|}$ with angle $\phi = -\gamma \| \mathbf{B}_{\mathrm{eff},t} \| \Delta t$. For a spin at location \mathbf{r} , this effective magnetic field is $\mathbf{B}_{\mathrm{eff},t}(\mathbf{r}) = \kappa(\mathbf{r})\mathbf{b}_t + (\mathbf{g}_t \cdot \mathbf{r} + \Delta B(\mathbf{r}))\mathbf{\hat{z}}$, where $\Delta B(\mathbf{r})$ represents the off-resonance caused by the field inhomogeneity and chemical shift, and $\kappa(\mathbf{r})$ represents the scale factor that accounts for the inhomogeneous RF transmit (\mathbf{B}_1^+) field.

The simulation of the spin-domain representation was implemented in *PyTorch*. To reduce computation time and memory use for the optimization, we implemented the explicit Jacobian operation of the final spin-domain representation α_T and β_T with respect to α_t and δ_t , detailed in Section A of the Supporting Information. Other partial derivatives, such as $\partial \mathcal{L}/\partial(a_t, b_t)$, $\partial(a_t, b_t)/\partial \mathbf{g}_t$ and $\partial(a_t, b_t)/\partial \mathbf{b}_t$, which require less computation, were obtained directly by PyTorch using auto-differentiation. The use of auto-differentiation provided flexibility in formulating optimization problems with arbitrary loss functions. We evaluated the effectiveness of our spin-domain simulation with explicitly derived Jacobian by comparing it in terms of optimization time and memory use to a simulation that did not use an explicitly derived Jacobian. This comparison was performed on a Linux workstation equipped with an Intel Xeon w7-2475X CPU and an NVIDIA RTX A4000 graphics card.

3.2 | Optimization of RF and gradient waveforms

Optimized RF and gradient waveforms were generated by minimizing the loss function \mathcal{L} as defined in Eqs. (8) and (9) for refocusing and excitation pulses, starting from given initial \mathbf{b}_{init} and \mathbf{g}_{init} . The design variables \mathbf{b} and \mathbf{g} were updated alternately using an alternating minimization algorithm, outlined in Algorithm 1, which is based on Frank Wolfe³⁶ and gradient descent, detailed in Section B of the Supporting Information). Constrained optimization was used to ensure that the updates to \mathbf{b} and \mathbf{g} remained feasible.

In this study, the initial \mathbf{b}_{init} and \mathbf{g}_{init} were designed using a multidimensional small-tip-angle excitation

pulse-design algorithm¹⁶ that optimizes the RF waveform and a continuous excitation k-space trajectory (extended KT-points trajectory) based on the desired 3D excitation pattern. These initial waveforms were designed to excite the ROI with a 30° flip angle while satisfying the hardware constraints. The same initialization was used for both excitation and refocusing designs. To balance the optimization effort on the spins in the ROI and the outer volume (OV), we chose the weight functions to as the ratio of the reciprocal of the total number of spins in each region. RF pulses with various ROI sizes were designed for the phantom and in vivo experiments. The excitation pulse was designed to be applied along the y-axis, whereas the refocusing pulse was designed to be applied along the y-axis. The values of b_{max} = 14 µT, g_{max} = 50 mT/m, and s_{max} = 120 mT/m/ms were used as the optimization constraints.

To evaluate the performance of the optimized 3D excitation and refocusing pulses, the root mean squared error (RMSE) between the simulated and desired target profiles was calculated. The performance of optimized 3D pulses was compared with their initializations and the small-tip designs¹⁶ that were scaled to target flip angles of 90° or 180°.

3.3 | RF pulse design with B_0 and B_1 ⁺ compensations

To assess the effectiveness of considering B_0 and B_1^+ on the pulse design and the resulting signal accuracy in the presence of such imperfections, 3D excitation and refocusing pulses designed with B_0 and B_1^+ were compared to the pulses without accounting for B_0 and B_1^+ inhomogeneities in the simulations. The transverse magnetization in the spin echo was approximated by multiplying 3D excitation and refocusing profiles. These pulses were designed for a ROI with dimensions of $8\times8\times6\,\mathrm{cm}^3$ on a $40\times40\times28$ voxel grid with a FOV of $30\times30\times10\,\mathrm{cm}^3$. Various simulated B_0 and B_1^+ maps were used in these simulations. RMSE was used to quantify the performance.

3.4 | Effect of RF and gradient initializations

To investigate the effect of the initialization on the optimization, we examined pulse optimization using different initializations for the RF waveforms. For the gradients, extended KT-points¹⁶ and SPINS⁴² were used as initializations. For the RF waveform, 30° small-tip-angle excitation and random values were used. The same optimization was performed. RMSE was used to quantify the performance.

3.5 | Effect of gradient updates during the optimization

To investigate the effect of gradient updates during the joint optimization, the 30° small-tip-angle excitations with extended KT-points and SPINS gradient trajectories were used as the initialization and optimized by (1) joint optimization of RF and gradient waveforms; and (2) RF-only optimization with fixed gradients.

3.6 | Effect of cost function on excitation optimization

For the 90° excitation pulse, the term of $|\beta_{T,i}(\mathbf{b}, \mathbf{g})| - |\beta_{D,i}|$ can be ignored for the cost function design. The effect of the choice of cost function on the excitation pulse optimization results was explored using an alternate cost function \mathcal{L}_s as shown in Eq. (10):

$$\mathcal{L}_{s} = \sum_{i=1}^{m} w_{i} \left| \alpha_{T,i}^{*}(\mathbf{b},\mathbf{g}) \beta_{T,i}(\mathbf{b},\mathbf{g}) - \frac{i}{2} e^{i\psi} \sin \theta_{i} \right|^{2} + \lambda ||\mathbf{b}||_{2}^{2}$$
 (10)

The effect of the regularization term was excluded by setting $\lambda = 0$. The 3D excitation pulses were optimized with two cost functions using the same weighting function and the same number of 10 iterations.

3.7 | Comparison with optimization using Bloch simulator

Our proposed 3D 90° excitation pulse optimization using the spin-domain simulator was compared with the pulse optimization of Luo et al.'s method,²⁶ which used a Bloch simulator²⁶ by designing 3D excitation for the same ROI. RMSE between the simulated and desired excitation profile was calculated to compare the performance. For the 3D refocusing pulse, to our knowledge, there is no existing method that designs 3D refocusing pulses with similar gradient trajectories. We compared the 3D 180° inversion pulse designed using Luo et al.'s method²⁶ with our optimized 3D refocusing pulse that was designed for the same ROI. The same initialization, spatial weighting, and system constraints were used for all the design experiments.

3.8 | Phantom experiments

All experiments were performed on a 3T scanner (Magnetom Vida; Siemens Healthineers, Erlangen, Germany). The B_0 map was estimated from gradient-echo (GRE) images with two echo times (TEs) of 2.51 ms and 4.84 ms

using a regularized estimation method.³⁷ The B_1^+ maps was acquired using a fast B_1^+ mapping method.³⁸ The acquisition time for B_0 map was 44 s for 34 slices, using a matrix size 128×128 with an FOV of $300 \times 300 \times 102$ mm³. For the B_1^+ map, the acquisition time was 19 s using a matrix size of 64×64 with the same FOV and the number of slices.

A spin-echo sequence with a 3D stack-of-echo-planar imaging (EPI) readout was implemented using Pulseq.³⁹ The 3D pulses designed with an ROI size of $8 \times 8 \times 6 \text{ cm}^3$ using our proposed algorithm were used to replace the conventional one-dimensional (1D) pulse in the spin-echo sequence. Because the spin-echo signal profile is affected by both excitation (90°) and refocusing (180°) pulses, we hypothesized that combining 3D 90° and 3D 180° pulses might produce better OV suppression. To investigate the optimal combination of excitation and refocusing pulses for ROI signal selection and OV suppression, we acquired images with the following configurations: (1) SINC excitation and refocusing (1D 90° + 1D 180°), (2) 3D excitation and SINC refocusing (3D 90° + 1D 180°), (3) SINC excitation and 3D refocusing (1D 90° + 3D 180°), and (4) 3D excitation and 3D refocusing (3D 90° +3D 180°). All images were acquired with a full FOV of $300 \times 300 \times 96 \text{ mm}^3$ with a TE of 64 ms and a repetition time of 1 s. The EPI readout used 75% partial Fourier sampling with an acceleration factor of 2. The scan time was 32 s for a spatial resolution of $2.34 \times 2.34 \times 3 \,\mathrm{mm}^3$. The coil-sensitivity maps were estimated from a GRE prescan using ESPIRiT.⁴⁰ The undersampled data were then reconstructed using sensitivity encoding,⁴¹ using these sensitivity maps. For the reduced FOV (rFOV) images, the sensitivity maps were cropped from the full FOV sensitivity maps to match the targeted imaging region.

3.9 | In vivo experiments

The study was approved by the institutional review board, and informed written consent was obtained from each participant. The sequences and parameters for in vivo experiments are summarized in Table S1. Both brain and prostate images were acquired with a matrix size of $128 \times 128 \times 32$, a repetition time of 1 s, and a TE of 64 ms. The 3D EPI readout had 75% partial Fourier with an undersampling rate of 2. The scan time for the 3D volume was 32 s per repetition.

Brain images were obtained in 2 subjects using a 20-channel head–neck receive coil array. The 3D excitation and refocusing pulses were designed for a ROI size of $6 \times 6 \times 6 \text{ cm}^3$. B_0 and B_1^+ maps were acquired for each subject. Images were acquired with a full FOV of $256 \times 256 \times 96 \text{ mm}^3$ (spatial resolution $2 \times 2 \times 3 \text{ mm}^3$) and a reduced FOV of $128 \times 128 \times 96 \text{ mm}^3$ (spatial resolution

 $1 \times 1 \times 3 \text{ mm}^3$), using either 1D pulses or the proposed 3D pulses, respectively. Additionally, reference images were acquired using two-dimensional (2D) turbo spin echo (TSE) with a TE of 61 ms and a spatial resolution of $1 \times 1 \times 3 \text{ mm}^3$.

Two subjects underwent prostate imaging using an 18-channel body array and a 32-channel spinal array. The 3D pulses for a ROI of $9 \times 9 \times 6$ cm³ were optimized using B_0 and B_1^+ maps measured in the pelvic region. Images were acquired with a full FOV of $384 \times 384 \times 96$ mm³ (spatial resolution $3 \times 3 \times 3$ mm³) and a reduced FOV of $128 \times 128 \times 96$ mm³ (spatial resolution $1 \times 1 \times 3$ mm³). Prostate images were acquired with two averages, resulting in a total scan time of 64 s to cover the entire 3D volume. An additional reference image was acquired using 2D TSE with a TE of 62 ms and a spatial resolution of $1 \times 1 \times 3$ mm³.

4 | RESULTS

4.1 | Spin-domain simulation using explicit Jacobians

Figure 1 compares computation time and memory use for calculating the derivative using our proposed explicit Jacobian formulation versus standard auto-differentiation. For simulating a RF pulse with 3000 time points and 10 000 spins, both approaches used about 3.8 GB of GPU memory. However, the auto-differentiation method without explicitly derived Jacobian required about 21.3 times longer computation time than our explicit Jacobian implementation. Although both simulators produced identical derivatives, the explicit Jacobian formulation demonstrates significant time efficiency, with performance advantage expected to scale further with increased number of spins or time points.

4.2 | RF pulse design with B_0 and B_1 ⁺ compensations

Our designed 3D excitation and refocusing pulses have the same durations of 4.15 ms. In the current experiment, optimizing each RF pulse took approximately 7 min with 10 iterations, with each iteration consisting of five updates to RF and five updates to gradient waveform. Figure S1 illustrates the design target and the weighting function for the phantom, as well as measured B_0 and B_1^+ maps of the phantom.

Figure 2 demonstrated the benefits of accounting for B_0 inhomogeneity in RF pulse design. When B_0 inhomogeneities are incorporated, excitation and refocusing accuracy remain preserved across varying B_0 field conditions

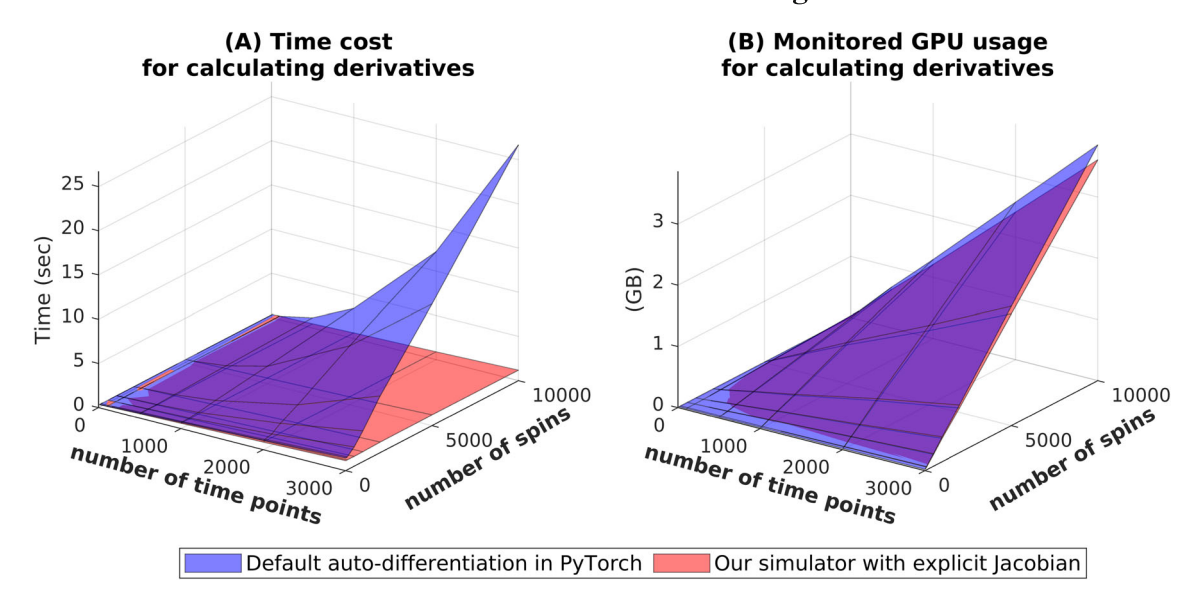


FIGURE 1 Compute time and memory use for derivative calculations comparing our implemented spin-domain simulator with explicitly derived Jacobians versus default auto-differentiation. Performance was evaluated while scaling the number of spins or time points in the simulation. Both approaches used for designing identical RF pulses and loss functions with derivatives were calculated once.

(Figure 2B). In contrast, designs neglecting B_0 exhibit significant degradation in accuracy. Furthermore, the combination of 3D excitation and refocusing pulses achieved the lowest RMSE in OV.

Figure 3 illustrates the benefit of incorporating B_1^+ inhomogeneity into RF pulse design. By including B_1^+ transmit maps, consistent RF accuracy is achieved across varying B_1^+ fields, whereas designs without B_1^+ compensation exhibit degradation in accuracy. Like the results with B_0 compensation, the combination of 3D excitation and refocusing pulses achieved the lowest RMSE in OV suppression.

Simulations with inhomogeneous B_0 and B_1^+ fields show that RF pulses designed with these inhomogeneities accounted for better performance than those designed without them. With the ROI weighted more heavily than the OV, B_0 and B_1^+ compensation consistently reduced RMSE within the ROI across all experiments. The results also suggest that 3D refocusing pulses may outperform 3D excitation pulses in suppressing OV signals, whereas the combined use of both 3D excitation and refocusing pulses achieved the lowest RMSE values overall.

The performance of optimized 3D excitation and refocusing pulses, compared with scaled small-tip-angle designs, is shown in Figures S2–S5. These RF pulses were designed with measured B_0 and B_1^+ maps of the phantom (Figure S1). For excitation, the optimized 3D pulse (Figure S2) achieves a lower peak RF amplitude than the scaled 90° pulse. Its simulated profile (Figure S3) also yields a smaller RMSE within the ROI (0.03 vs. 0.10). Similarly, the optimized 3D refocusing pulse (Figure S4)

demonstrates a reduced peak RF compared with the scaled 180° pulse, with its corresponding simulated profile (Figure S5) showing a smaller RMSE (0.06 vs. 0.24).

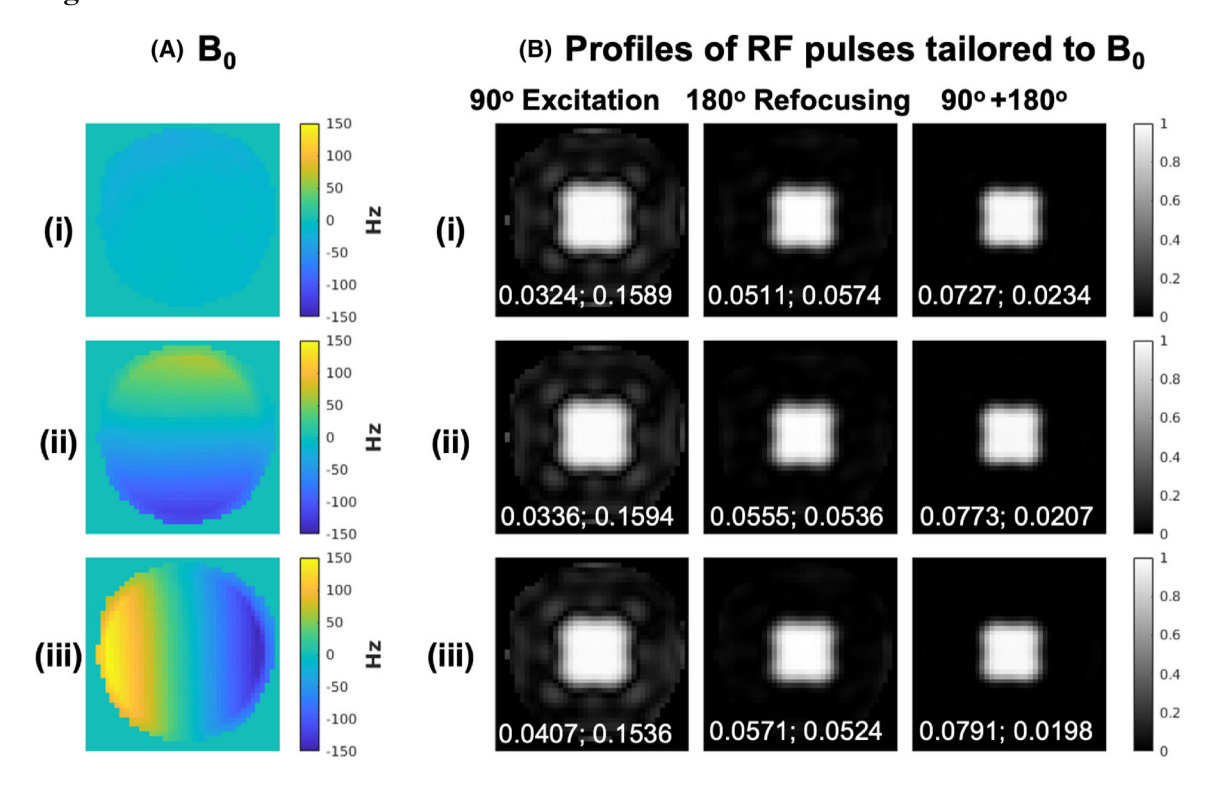
Figures S6 and S7 evaluate the trade-offs between pulse performance and computational efficiency. Figure S6 illustrates the convergence behavior of the cost function and RMSE during optimization. Figure S7 shows that reducing the optimization time from 7 min to 3 min results in negligible RMSE differences (<0.02) in simulated pulse performance. These findings suggest that iterations can be reduced in practice, either by adopting shorter optimization thresholds or redefining convergence criteria, to reduce computation without sacrificing performance.

4.3 | Effect of RF and gradient initializations

Figure S8 shows the initialization of RF and gradient waveforms within gradients based on extend KT-points. Figure S9 shows the corresponding initializations using SPINS for gradients. The RF waveforms were initialized with either a 30° 3D excitation or random values. Figure S10 compares the convergence behavior of the cost function and RMSE within the ROI during the optimization. Figure S11 evaluates the performance of different initial pulses before and after optimization. Although different initial RF waveforms resulted in nearly identical final performance (RMSE difference < 0.01), the choice of initial gradient waveforms had a more substantial influence on the optimized outcome.

0.4

0.1218; 0.0319



90° Excitation 180° Refocusing 90°+180° 0.6 (i) 0.4 0.2 0.0699; 0.0580 0.0816; 0.0236 0.1696; 0.1604 0.6 (ii) 0.4 0.2 0.1445; 0.0239 0.3873; 0.1836 0.1417; 0.0601 0.6 (iii)

0.1119; 0.0758

(c) Profiles of RF pulses designed without B₀

FIGURE 2 Impact of B_0 field inhomogeneity on radiofrequency (RF) pulse accuracy. (A) Three different B_0 maps acquired via manual shim adjustments (center slice shown for each). (B) Simulated results for excitation, refocusing pulses and the combination of excitation, and refocusing pulses designed with B_0 field compensation. (C) Simulated results for RF pulses designed without B_0 compensation. Root mean square error (RMSE) between simulations and target profiles was calculated over the region of interest (ROI) and outer volume (OV). B_0 -compessated designs yielded lower RMSE, with combined excitation-refocusing pulses further improving OV suppression.

0.3808; 0.2072

RMSE of ROI, OV -

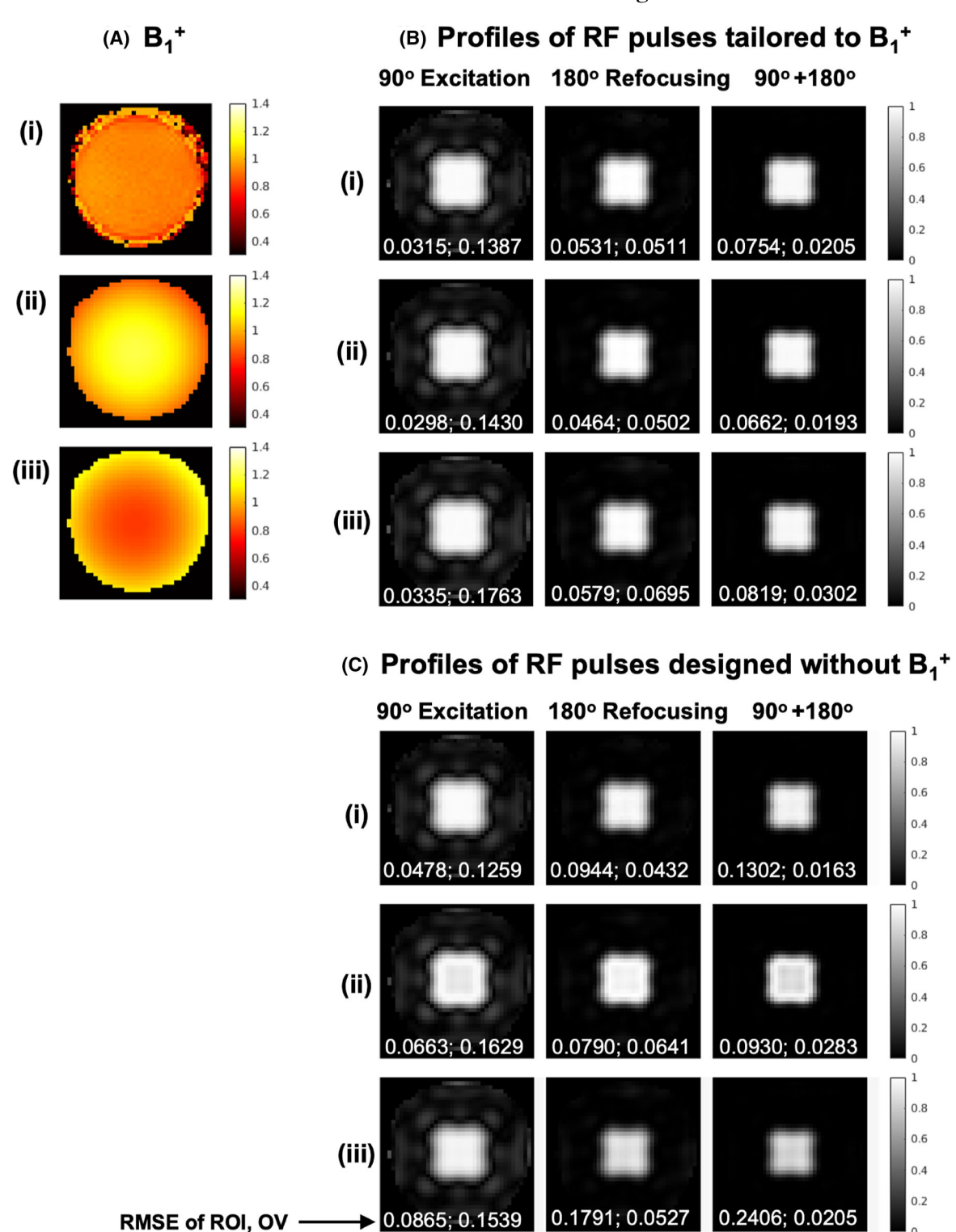


FIGURE 3 Impact of B_1^+ inhomogeneity on radiofrequency (RF) pulse accuracy. (A) Three simulated B_1^+ maps (center slice shown for each). (B) Simulated slice profile for excitation, refocusing pulses, and the combination of three-dimensional excitation and refocusing pulses designed with B_1^+ compensation. (C) Simulated profile for pulses designed without B_1^+ compensation. Root mean square error (RMSE) between simulated and target profiles was calculated over the region of interest (ROI) and outer volume (OV). B_1^+ compensated designs achieved lower RMSE, with the combined application of excitation and refocusing pulses further enhancing OV suppression.

4.4 | Effect of gradient updates during the optimization

Figures S12–S14 compare the performance of joint RF and gradient optimization against RF-only optimization (with fixed gradients). For gradients initialized using extended KT-points, both optimizations achieved comparable final performance, with RMSE values of 0.057 and 0.061 (Figure S13). However, for gradients initialized using SPINS, RF-only optimization showed limited improvement (Figure S12) and resulted in a higher RMSE (0.32) compared with joint optimization (RMSE 0.14). This result illustrates the need of joint RF and gradient optimization when the initial gradient waveforms are not well-designed for the target RF pulse. Figure S14 further illustrates that joint optimization was able to adjust gradient waveforms to improve the performance.

4.5 | Effect of cost function on excitation optimization

Figure S15 compares the optimized RF waveforms generated using two different cost functions for the 3D excitation pulse, and Figure S16 compares their convergence behaviors. Both cost functions \mathcal{L} (Eq. 9) and \mathcal{L}_s (Eq. 10) decreased with similar speed. However, \mathcal{L}_s , without the β magnitude term, yielded a RMSE of 0.06 within the ROI and 0.12 in the OV. In contrast, \mathcal{L} , with the β magnitude term, achieved a lower RMSE within ROI (0.02) but a slightly higher RMSE in OV (0.14). These results demonstrate that the inclusion of the β magnitude term improved RF performance within the ROI.

4.6 | Comparison with optimization using Bloch simulator

Figures S17–S20 compare spin-domain optimization and auto-differentiable Bloch simulations²⁶ for designing 3D excitation and refocusing pulses. Figure S17 shows the excitation profiles corresponding to the RF and gradient waveforms shown in Figure S18. Although the Bloch simulation–based method achieved lower RMSE across the entire object (0.08 vs. 0.12 for spin domain), the proposed spin-domain optimization exhibited a lower RMSE within the ROI (0.11 vs. 0.12 for Bloch).

For the 3D refocusing pulses, Figure S19 shows the refocusing profiles corresponding to the RF and gradient waveforms in Figure S20. The refocusing pulse designed using spin-domain optimization had an RMSE of 0.07 for the magnitude of β^2 , whereas the Bloch simulation–based inversion pulse achieved a lower RMSE of 0.03.

However, the spin domain-optimized refocusing pulse showed reduced phase variation within the ROI (Figure S19), which is important for ensuring that the refocusing pulse uniformly inverts the phase of spins across the ROI without introducing spurious phase offsets.

4.7 | Phantom experiments

Figure 4 presents the designed 3D excitation and refocusing pulses along with the spin-echo 3D EPI sequence used in this study. The sequence includes a fat-saturation module to suppress fat signals and a three-line navigator to correct for phase discrepancies between odd and even lines in EPI data.

Figure 5 compares the signal profiles acquired with different combinations of excitation and refocusing pulses. Receiver field heterogeneity was corrected via a GRE-based prescan normalization. Phantom results closely matched simulations, validating the performance of our optimized 3D pulse designs. Notably, the combination of 3D 90° and 3D 180° pulses achieved the most effective OV signal suppression compared with the other configurations.

Figure 6 further compares the 1D profiles of the measured signal intensity along different directions of the object. The combination of 3D 90° and 3D 180° exhibited the lowest OV signal. This outcome demonstrates that using two 3D pulses can achieve higher spatial selectivity, effectively minimizing signal contributions from outside the ROI.

4.8 | In vivo experiments

Figure 7 shows B_0 and B_1^+ maps, images acquired with 3D EPI sequence with various configurations, alongside T_2 -weighted 2D TSE images of a healthy subject's brain. The rFOV acquisition achieved higher spatial resolution $(1 \times 1 \times 3 \text{ mm}^3)$ compared with full FOV images $(2 \times 2 \times 3 \text{ mm}^3)$ while maintaining identical scan time (32 s).

Figure 8 shows B_0 and B_1^+ maps, images acquired with 3D EPI sequence with various configurations, alongside T_2 -weighted 2D TSE images of the prostate of a healthy subject. The rFOV images (acquired using 3D $90^\circ + 3D$ 180° pulses) achieved $1 \times 1 \times 3$ mm³ spatial resolution, 3-fold higher in-plane than the full FOV ($3 \times 3 \times 3$ mm³), while maintaining the same scan time (64s) and exhibiting reduced geometric distortion as validated by alignment with reference 2D TSE images. Discrepancies in full FOV zoomed views (e.g., anatomical misregistration, marked by red arrows/bars) underscore the advantage of the rFOV approach in balancing resolution and geometrical

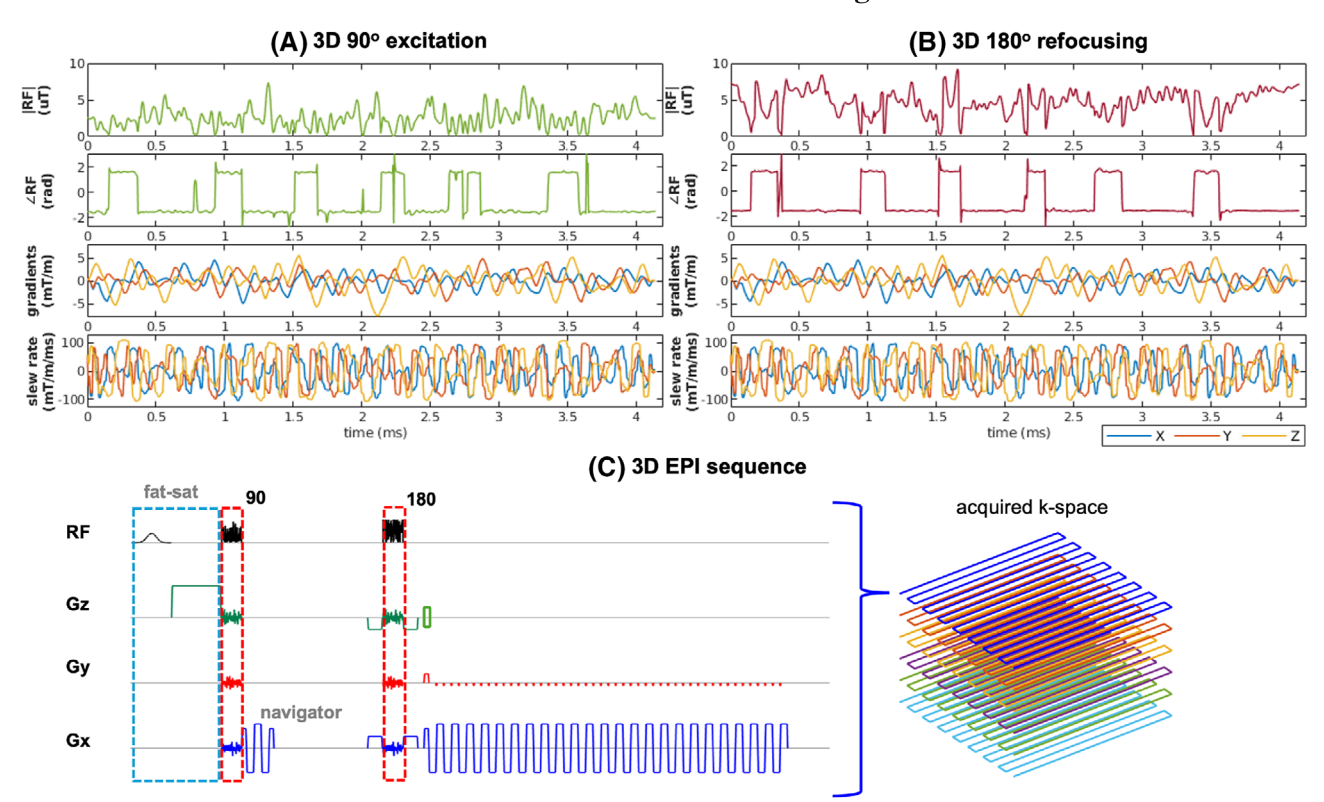


FIGURE 4 Optimized three-dimensional (3D) excitation and refocusing radiofrequency (RF) pulses and pulse sequence diagram. (A) RF and gradient waveforms of the optimized 3D 90° excitation pulse. (B) RF and gradient waveforms of the optimized 3D 180° refocusing pulse. (C) The 3D echo-planar imaging (EPI) sequence diagram incorporating 3D excitation and refocusing pulses. The sequence includes a fat-saturation module at the beginning and a three-line navigator after the excitation to correct the phase of odd and even lines in EPI data.

distortion for prostate imaging. Results in both Figures 7 and 8 demonstrate the potential of the rFOV approach to improve the spatial resolution without compromising acquisition efficiency.

Figure 9 quantifies OV suppression across pulse configurations using relative OV signal intensity, defined as follows:

 $= \frac{\text{average outer volume signal intensity}}{\text{average ROI signal intensity}}$

The 3D $90^{\circ} + 3D$ 180° pulse combination with B_0 and B_1^+ compensations achieved the most effective OV signal suppression, with the relative OV signal values of 0.02 in the brain and 0.06 in the prostate. However, improvements from B_0 and B_1^+ compensations was modest, likely due to the short pulse duration that is less sensitive to off-resonance, and limited B_1^+ variation within the small ROI.

5 | DISCUSSION

In this study, we developed a novel algorithm for designing multidimensional RF pulses using the spin-domain

representation, which jointly optimizes RF and gradient waveforms. This approach accounts for B₀ and B₁⁺ inhomogeneities as well as system hardware limitations, such as peak RF power, maximum gradient strength, and maximum gradient slew rate, by solving a constrained optimization problem. The spin-domain representation simplifies the cost function of the refocusing pulse design problem. Therefore, our algorithm does not require explicit knowledge of the initial or target magnetization of individual spin isochromats. To reduce computation time, we implemented auto-differentiation with explicitly derived Jacobians. The auto-differentiable simulation function also incorporates B₀ and B₁⁺ field inhomogeneities, simplifying their integration into the optimization. Although this study was primarily motivated by designing 3D refocusing pulses for spin echo-based sequences, we also demonstrated the potential of using our method to design other RF pulses, such as 3D excitation pulses.

Our algorithm works with arbitrary excitation k-space trajectories and is not limited to, for example, spirals or EPI, as often done in previous works. This feature enables the design of 3D pulses to have shorter pulse duration compared with pulses using spiral or EPI. The short pulse duration (4.15 ms) provides flexibility in replacing the conventional 1D pulses with these 3D pulses in our

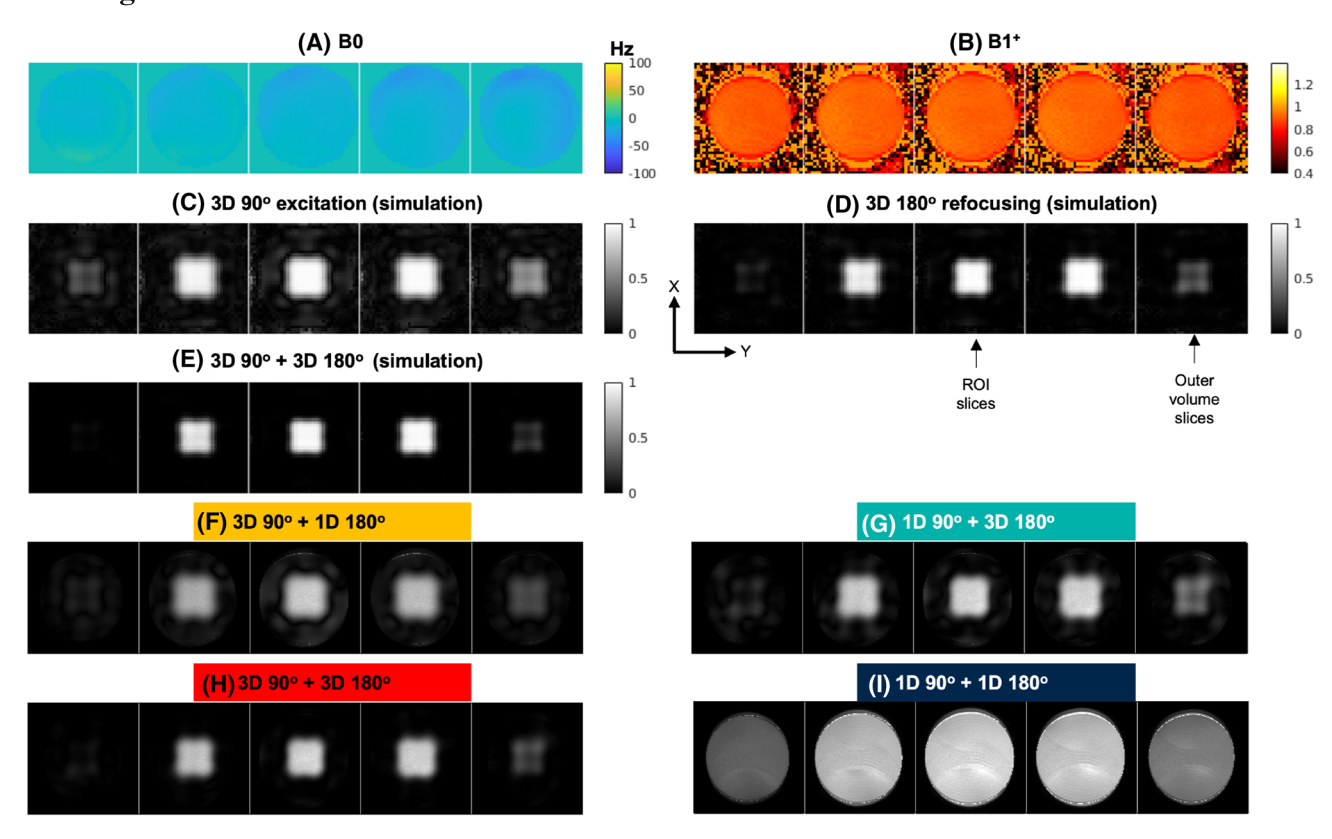
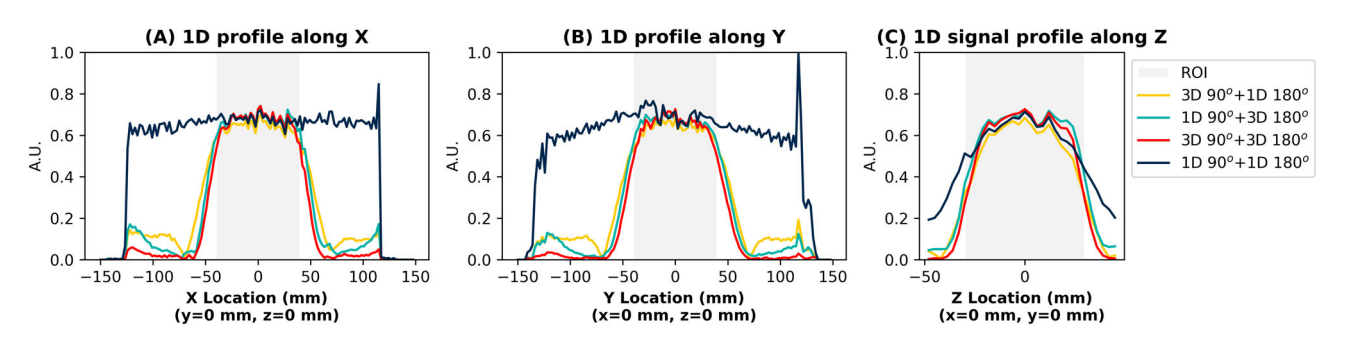


FIGURE 5 Simulated and experimental spin-echo signal profiles for various combinations of selective excitation and refocusing pulses. (A) B₀ map. (B) B₁⁺ map of the phantom. (C-E) Simulated slice profiles (slice positions: -36, -18, 0, 18, and 36 mm) for three-dimensional (3D) excitation, 3D refocusing, and their combined application. (F-I) Phantom images acquired using one-dimensional (1D)/3D excitation/refocusing pulse combinations. The acquired 3D images closely match simulated results, validating the radiofrequency pulse design. ROI, region of interest.



Comparison of spin-echo signal profiles across spatial axes (x, y, and z) in the phantom. The combined application of three-dimensional (3D) excitation and refocusing pulses improved the outer-volume signals suppression in all three dimensions compared with other pulse configurations. 1D, one-dimensional; ROI, region of interest.

current pulse sequence implementation. In this study, we inserted 3D excitation and refocusing pulses into a spin-echo sequence with a 3D stack-of-EPI acquisition to evaluate the performance of our design algorithm. We demonstrated improved spatial selectivity by using two 3D pulses together, compared with a combination of one 1D and one 3D pulse. When comparing the spatial selectivity among different pulse configurations, our results show that the 3D refocusing pulses have better performance than the 3D excitation pulses, possibly due to the presence of crusher gradients with the refocusing pulses and the choices of the cost functions. The β^2 term in the cost function for the refocusing pulses effectively models the refocusing performance with crushers, whereas the cost function chosen for excitation may have been suboptimal. For excitation pulse, an alternate cost function without β magnitude term for the 90° excitation pulse optimization was explored. We noticed that the cost function decreased

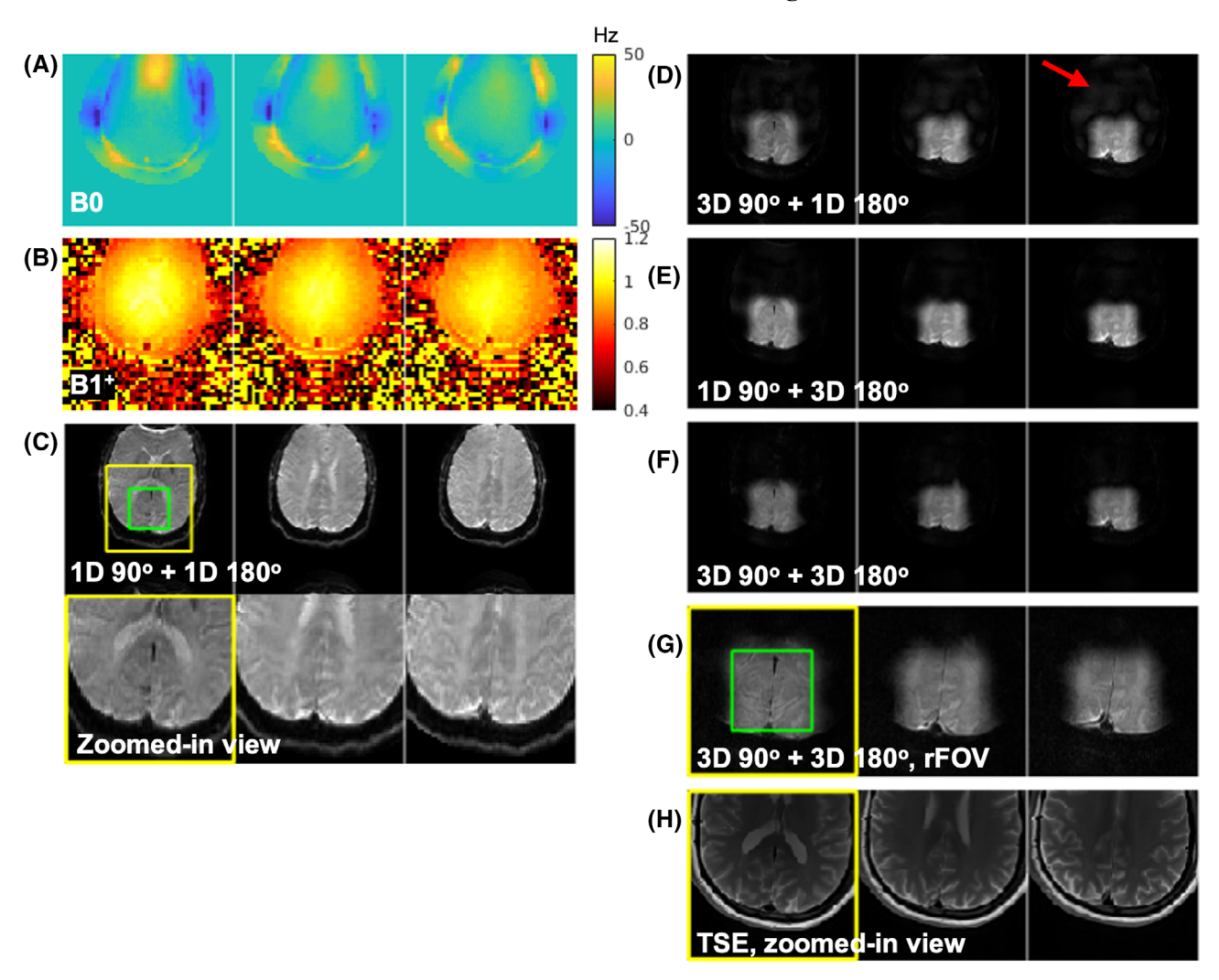


FIGURE 7 In vivo brain imaging results (3 representative slices out of 32 shown per subfigure). (A) B_0 off-resonance map. (B) B_1^+ map. (C-F) Full field of view (FOV) (300 × 300 × 96 mm³) three-dimensional (3D) spin-echo images acquired using a stack-of-echo planar imaging using one-dimensional (1D) 90° + 1D 180° (C), 3D 90° + 1D 180° (D), 1D 90° + 3D 180° (E), and 3D 90° + 3D 180° (F) pulse configurations. The 3D 90° + 1D 180° combination produced higher outer-volume (OV) signal than the others ($red\ arrow$). (G) Reduced FOV (rFOV) (128 × 128 × 96 mm³) images acquired using 3D 90° + 3D 180°. (I) Zoomed reference two-dimensional turbo spin-echo (TSE) images (128 × 128 × 96 mm³). The region of interest (ROI) (6 × 6 × 6 cm³) is indicated by the green box, and rFOV is indicated by the yellow box. The slightly larger rFOV accommodates a transition region between ROI and OV during optimization. The rFOV acquisition (G) achieved 1 × 1 × 3 mm³ resolution compared with the full rFOV (C) (2 × 2 × 3 mm³) with identical scan time (32 s), demonstrating effectiveness of rFOV imaging in improving acquisition efficiency.

with similar speed for two different cost functions. However, it gave different excitation pulse solutions, leading to different ROI and OV performance. In the future study, it would be beneficial to explore other design formulations for the excitation design, such as magnitude least squares design.⁴³

Our study has several limitations. The spin-domain representation does not incorporate relaxation effects. However, given that the pulse durations in our experiments are shorter than typical tissue-relaxation times, their effect could be small. When designing RF pulses with

longer durations, it would be helpful to verify the results using Bloch simulations that account for relaxation effects.

Although our proposed optimization included B_0 and B_1^+ compensation, the improvements in in vivo experiments were small. This may stem from the short pulse duration, which inherently reduces sensitivity to B_0 inhomogeneity, and the small flip-angle excitation in the OV that limits the effect of B_1^+ inhomogeneity. As a result, the effectiveness of B_0 and B_1^+ compensation was primarily validated in simulation experiments. Additionally, our current work did not include B_1^+ phase information; however,

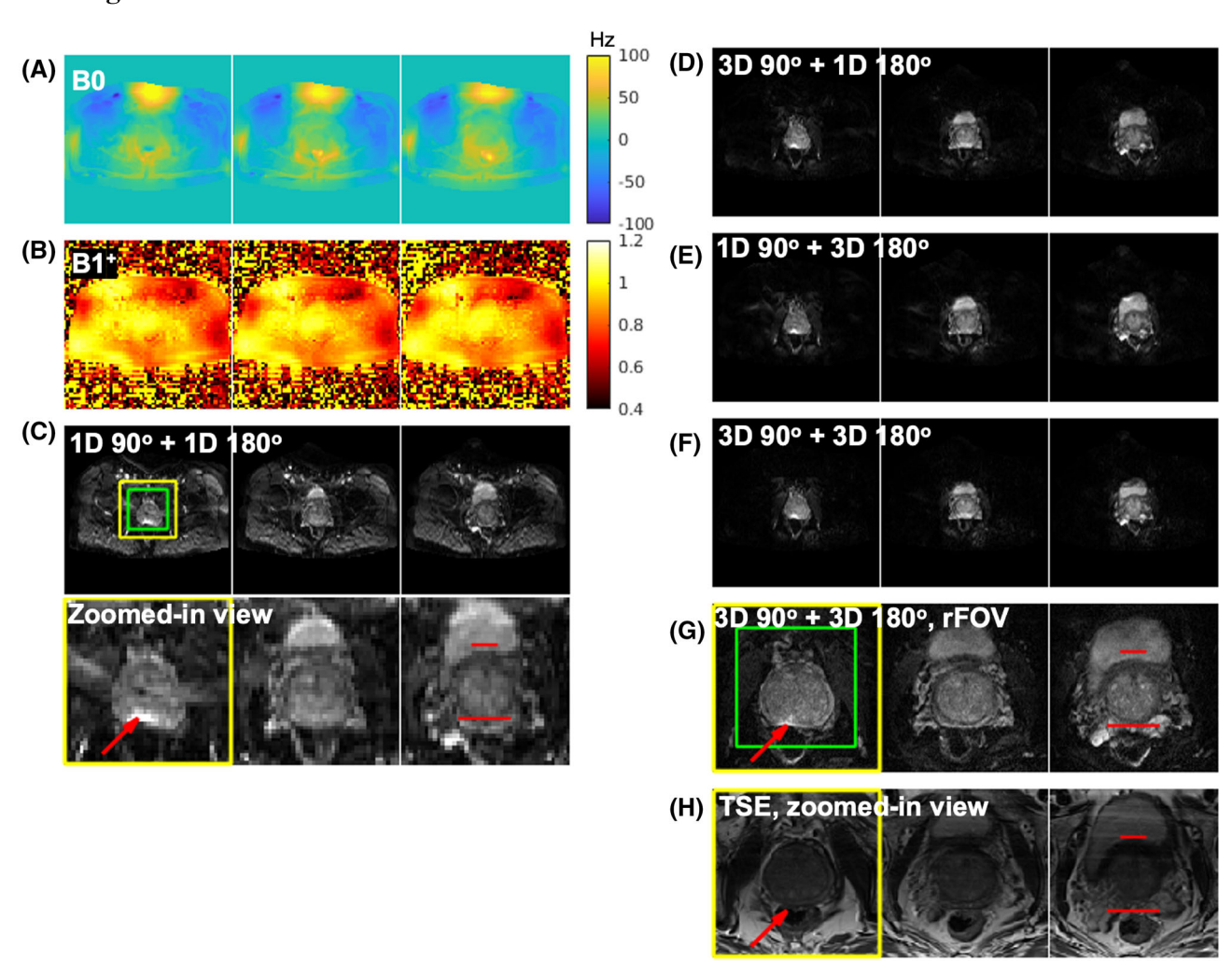


FIGURE 8 In vivo prostate imaging results (3 representative slices out of 32 shown). (A) B_0 off-resonance map. (B) B_1^+ map. (C-F) Full field of view (FOV) (384 × 384 × 96 mm³) three-dimensional (3D) spin-echo prostate images (3 × 3 × 3 mm³ resolution) acquired a stack-of-echo-planar imaging sequence using one-dimensional (1D) 90° + 1D 180° (C), 3D 90° + 1D 180° (D), 1D 90° + 3D 180° (E), and 3D 90° + 3D 180° (F) configurations. (G) Reduced FOV (rFOV) (128 × 128 × 96 mm³) 3D spin-echo images (1 × 1 × 3 mm³ resolution) acquired with 3D 90° + 3D 180°. (H) Zoomed reference 2D turbo spin-echo (TSE) images. The region of interest (ROI; green box) and rFOV (yellow box) are annotated. The rFOV images (G) exhibit reduced geometric distortion compared with full-FOV zoomed views, as illustrated by alignment with TSE reference images (discrepancies marked by red arrows and bars).

if the phase of B_1^+ is provided, our algorithm can easily include it into the spin-domain simulation function.

We observed slightly differences in image contrast between our rFOV images and conventional 2D TSE images, despite using similar TEs. Three factors may contribute to this discrepancy in contrast: First, the extended spin-echo train in TSE and the gradient echo training in 3D EPI for rFOV images may introduce slightly different T₂ and T₂* weightings. Second, differences in RF pulses (e.g., amplitude, duration, number of pulses) between two sequences could lead to different magnetization transfer effects,⁴⁴ altering tissue contrast. Third, stronger crusher gradients in the rFOV sequence, compared with full FOV TSE, likely increase diffusion sensitivity, further modifying image contrast. Although the impact of 3D pulse on

image contrast was not the focus of this study, these effects should be systematically investigated in future work.

Our current algorithm likely finds a local minimizer of the nonconvex design problem that depends on the RF and gradient initialization. The search for globally optimal (or at least more globally optimal) solutions is an open problem in multidimensional RF pulse design in general. One possible idea is to adopt strategies such as grid search⁴⁵ with different resolutions, although the large number of variables ($5 \times N_t$ for RF and gradient waveform) in our design problem could bring computation challenges. Another possible idea is to use inexact updates⁴⁶ to escape the local minimizers. The likelihood of falling into a local minimum seems particularly high for the gradient waveforms, because each gradient update

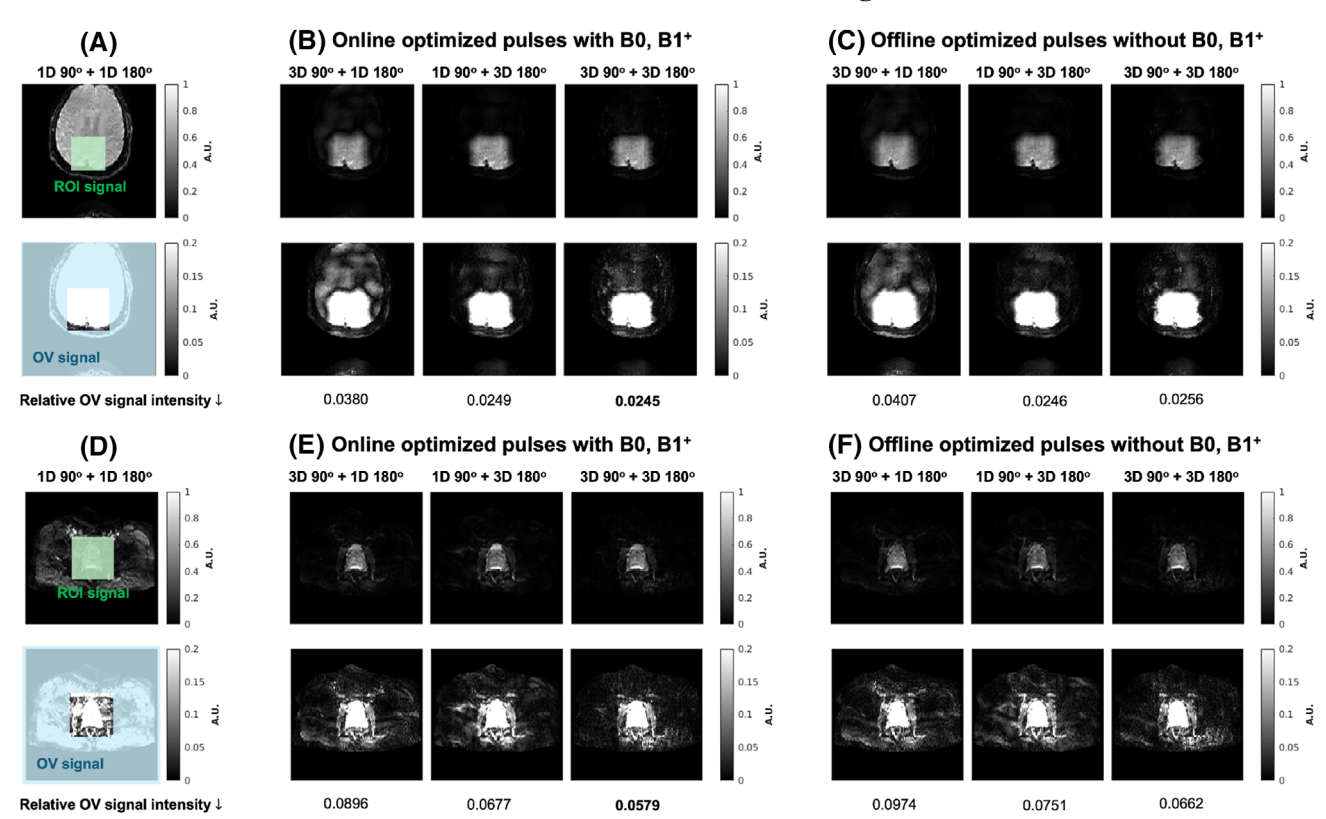


FIGURE 9 Outer-volume (OV) signal-suppression performance across various radiofrequency (RF) pulse configurations. (A) Brain image using one-dimensional (1D) $90^{\circ} + 1D$ 180° with annotated region of interest (ROI) and OV. (B) Brain images with optimized RF pulses with B_0 and B_1^+ compensations. (C) Brain images with RF pulses designed without B_0 or B_1^+ compensation. (D) Prostate image using 1D $90^{\circ} + 1D$ 180° with annotated ROI and OV. (E) Prostate images using optimized RF pulses with B_0 and B_1^+ compensations. (F) Prostate images with RF pulses designed without B_0 or B_1^+ compensation. Relative OV signal intensity is listed to quantify the OV suppression across these pulse configurations.

is limited to small changes, as we use constrained optimization to ensure that the solution is feasible with respect to MRI scanner hardware specifications. The initialization of RF waveform has a negligible effect on the results compared with the gradients, as shown by exploring different initializations of RF waveform. The limited updates to gradient waveforms during the optimization suggest that predefining good initial gradients and fixing them during the optimization is practical, reducing computation time. For the pulse design initialized with SPINS trajectory, joint RF and gradient optimization improved performance, as the SPINS-initialized gradients were suboptimal for the target pulse. To further improve the algorithm's performance, future studies could explore different initialization methods to seek globally optimal solutions. Additionally, incorporating constraints such as the symmetry in the excitation k-space, 47 by initializing symmetric trajectories and updating only half the gradient variables, could mitigate off-resonance effects for the refocusing pulse.

We compared our algorithm with the method that used an auto-differentiable Bloch simulator,²⁶ as, to our knowledge, no existing method designs 3D selective refocusing pulses with similar gradient trajectories. For the 3D excitation pulse, our proposed method achieved results comparable to the Bloch simulator. However, they do not lead to the same solution due to differences in cost functions and the optimization methods, which might lead to different local solutions of the nonconvex problem. For the 3D refocusing pulse, our algorithm produced a uniform phase profile within the ROI, which is important for spin-echo formation. In contrast, the 180° inversion pulse designed using the auto-differentiable Bloch simulator²⁶ exhibited greater phase variation. These results demonstrated the effectiveness of the cost function using spin-domain representation for designing multidimensional refocusing pulse, particularly in achieving phase coherence within the ROI

Our method is similar to optimal control (OC) pulse designs^{22,24} when considering the spin-domain representation as the system state to be controlled. However, instead of updating the control variables, such as RF and gradient waveforms in optimal control theory, we used the auto-differentiation framework to directly calculate derivatives of input variables with respect to

arbitrary loss functions. Although we explicitly derived Jacobian operations for the spin-domain simulation function, we treated it as an "encapsuled" function within the auto-differentiation framework. Future work could integrate OC approaches for minimum-time or minimum-energy solutions for the 3D pulse design.

In this work, as a proof of the concept, the number of optimization iterations was empirically chosen to limit the computation time to 16-20 min for two RF pulses—a duration still impractical for most in vivo experiments. In our experiments, the cost function decreased rapidly within the first 3 min (Figure S7), suggesting that early stopping, by monitoring pulse performance during the iterations, could shorten optimization time without compromising results. Additional strategies, such as fixed gradients (as discussed earlier) and alternative optimization methods (e.g., sequential quadratic programming⁴⁸ or acceleration with momentum⁴⁹), could further speed up the optimization. Using larger time steps for simulating RF and gradient waveforms can also accelerate the optimization, although this may lead to less accurate designs. Future work could extend this algorithm to design universal pulses^{47,50-52} that are robust to B₀ and B₁⁺ inhomogeneities, eliminating the need for subject-specific B₀ and B₁⁺ measurements. This approach would enable offline pulse optimization, saving total scan time.

6 | CONCLUSIONS

This paper presents a novel algorithm for designing multidimensional RF pulses using the spin-domain representation. By leveraging auto-differentiation with explicit Jacobian calculations, the algorithm accelerates derivative computation for cost function optimization, enabling efficient design of both 3D refocusing and excitation pulses. We demonstrated its application to reduced FOV imaging using numerical simulations and phantom and in vivo experiments.

ACKNOWLEDGMENTS

This work was supported in part by the National Institutes of Health under Award Numbers R01CA284172, R01EB032378, and R37CA263583 and by Siemens Healthineers. Jiayao Yang and Yun Jiang received research grant support from Siemens Healthineers.

DATA AVAILABILITY STATEMENT

The source code for this work is publicly available (https://github.com/MIITT-MRI-Jianglab/Multid_RF_SpinDomain).

ORCID

Jiayao Yang https://orcid.org/0009-0009-5046-1757

Jon-Fredrik Nielsen https://orcid.org/0000-0002-2058

-3579

Jeffrey A. Fessler https://orcid.org/0000-0001-9998-3315 Yun Jiang https://orcid.org/0000-0002-0713-9641

REFERENCES

- Rieseberg S, Frahm J, Finsterbusch J. Two-dimensional spatially-selective RF excitation pulses in echo-planar imaging. Magn Reson Med. 2002;47:1186-1193. doi:10.1002/mrm.10157
- Saritas EU, Cunningham CH, Lee JH, Han ET, Nishimura DG. DWI of the spinal cord with reduced FOV single-shot EPI. Magn Reson Med. 2008;60:468-473. doi:10.1002/mrm.21640
- Sun K, Zhong Z, Dan G, Karaman M, Luo Q, Zhou XJ. Three-dimensional reduced field-of-view imaging (3D-rFOVI). Magn Reson Med. 2022;87:2372-2379. doi:10.1002/mrm.29121
- Feinberg DA, Hoenninger JC, Crooks LE, Kaufman L, Watts JC, Arakawa M. Inner volume MR imaging: technical concepts and their application. *Radiology*. 1985;156:743-747. doi:10.1148/radiology.156.3.4023236
- Yang GZ, Gatehouse PD, Keegan J, Mohiaddin RH, Firmin DN. Three-dimensional coronary MR angiography using zonal echo planar imaging. *Magn Reson Med.* 1998;39:833-842. doi:10.1002/mrm.1910390521
- Smith TB, Nayak KS. Reduced field of view MRI with rapid, B1-robust outer volume suppression. Magn Reson Med. 2012;67:1316-1323. doi:10.1002/mrm.23116
- Alley MT, Pauly JM, Sommer FG, Pelc NJ. Angiographic imaging with 2D RF pulses. Magn Reson Med. 1997;37:260-267. doi:10.1002/mrm.1910370220
- Katscher U, Börnert P, Leussler C, Van Den Brink JS. Transmit SENSE. Magn Reson Med. 2003;49:144-150. doi:10.1002/mrm.10353
- Graesslin I, Biederer S, Schweser F, Zimmermann K, Katscher U, Börnert P. SAR reduction for parallel transmission using VERSE and k-space filtering. *Proceedings of the Annual Meeting of ISMRM*; 2007:674.
- Saekho S, Yip C, Noll DC, Boada FE, Stenger VA. Fastk z three-dimensional tailored radiofrequency pulse for reduced B1 inhomogeneity. *Magn Reson Med.* 2006;55:719-724. doi:10.1002/mrm.20840
- Lattanzi R, Sodickson DK, Grant AK, Zhu Y. Electrodynamic constraints on homogeneity and radiofrequency power deposition in multiple coil excitations. *Magn Reson Med*. 2009;61:315-334. doi:10.1002/mrm.21782
- Pauly J, Nishimura D, Macovski A. A k-space analysis of small-tip-angle excitation. J Magn Reson. 1989;81:43-56. doi:10.1016/0022-2364(89)90265-5
- Yip C, Fessler JA, Noll DC. Advanced three-dimensional tailored RF pulse for signal recovery in T2 *-weighted functional magnetic resonance imaging. Magn Reson Med. 2006;56:1050-1059. doi:10.1002/mrm.21048
- Yip C, Grissom WA, Fessler JA, Noll DC. Joint design of trajectory and RF pulses for parallel excitation. *Magn Reson Med*. 2007;58:598-604. doi:10.1002/mrm.21262
- Shao T, Xia L, Tao G, Chi J, Liu F, Crozier S. Advanced three-dimensional tailored RF pulse design in volume selective

- parallel excitation. *IEEE Trans Med Imaging*. 2012;31:997-1007. doi:10.1109/TMI.2011.2178035
- Hao S, Fessler JA, Noll DC, Nielsen JF. Joint design of excitation k-space trajectory and RF pulse for small-tip 3D tailored excitation in MRI. *IEEE Trans Med Imaging*. 2016;35:468-479. doi:10.1109/TMI.2015.2478880
- 17. Schröder C, Börnert P, Aldefeld B. Spatial excitation using variable-density spiral trajectories. *Magn Reson Imaging*. 2003;18:136-141. doi:10.1002/jmri.10334
- Yip C, Fessler JA, Noll DC. Iterative RF pulse design for multidimensional, small-tip-angle selective excitation. *Magn Reson Med*. 2005;54:908-917. doi:10.1002/mrm.20631
- Stenger VA, Boada FE, Noll DC. Multishot 3D slice-select tailored RF pulses for MRI. Magn Reson Med. 2002;48:157-165. doi:10.1002/mrm.10194
- Saekho S, Boada FE, Noll DC, Stenger VA. Small tip angle three-dimensional tailored radiofrequency slab-select pulse for reduced B1 inhomogeneity at 3 T. Magn Reson Med. 2005;53:479-484. doi:10.1002/mrm.20358
- Conolly S, Nishimura D, Macovski A. Optimal control solutions to the magnetic resonance selective excitation problem. *IEEE Trans Med Imaging*. 1986;5:106-115. doi:10.1109/TMI.1986.4307754
- 22. Xu D, King KF, Zhu Y, McKinnon GC, Liang Z. Designing multichannel, multidimensional, arbitrary flip angle RF pulses using an optimal control approach. *Magn Reson Med.* 2008;59:547-560. doi:10.1002/mrm.21485
- 23. Grissom WA, Xu D, Kerr AB, Fessler JA, Noll DC. Fast large-tip-angle multidimensional and parallel RF pulse design in MRI. *IEEE Trans Med Imaging*. 2009;28:1548-1559. doi:10.1109/TMI.2009.2020064
- 24. Rund A, Aigner CS, Kunisch K, Stollberger R. Magnetic resonance RF pulse design by optimal control with physical constraints. *IEEE Trans Med Imaging*. 2018;37:461-472. doi:10.1109/TMI.2017.2758391
- 25. Paszke A, Gross S, Chintala S, et al. Automatic differentiation in PyTorch. https://openreview.net/forum?id=BJJsrmfCZ. Published online October 28, 2017. Accessed April 4, 2025.
- Luo T, Noll DC, Fessler JA, Nielsen JF. Joint design of RF and gradient waveforms via auto-differentiation for 3D tailored excitation in MRI. *IEEE Trans Med Imaging*. 2021;40:3305-3314. doi:10.1109/TMI.2021.3083104
- Martin JB, Srinivas SA, Vaughn CE, Sun H, Griswold MA, Grissom WA. Selective excitation localized by the Bloch–Siegert shift and a B1+ gradient. *Magn Reson Med.* 2022;88:1081-1097. doi:10.1002/mrm.29271
- 28. Zhang M, Arango N, Arefeen Y, et al. Stochastic-offset-enhanced restricted slice excitation and 180° refocusing designs with spatially non-linear ΔB_0 shim array fields. *Magn Reson Med.* 2023;90:2572-2591. doi:10.1002/mrm.29827
- Pauly J, Le Roux P, Nishimura D, Macovski A. Parameter relations for the Shinnar-Le Roux selective excitation pulse design algorithm (NMR imaging). *IEEE Trans Med Imaging*. 1991;10:53-65. doi:10.1109/42.75611
- Pang Y, Shen G, Zhang X. Two dimensional spatial selective Shinnar Le Roux pulse design for arbitrary k-trajectory. Proceedings of the 17th Annual Meeting of ISMRM; 2009:2598.
- Pauly J, Spielman D, Macovski A. Echo-planar spin-echo and inversion pulses. Magn Reson Med. 1993;29:776-782. doi:10.1002/mrm.1910290609

- 32. Pauly JM, Hu BS, Wang SJ, Nishimura DG, Macovski A. A three-dimensional spin-echo or inversion pulse. *Magn Reson Med.* 1993;29:2-6. doi:10.1002/mrm.1910290103
- Grissom WA, McKinnon GC, Vogel MW. Nonuniform and multidimensional Shinnar-Le Roux RF pulse design method. *Magn Reson Med.* 2012;68:690-702. doi:10.1002/mrm.23269
- 34. Ma C, Liang Z. Design of multidimensional Shinnar–Le Roux radiofrequency pulses. *Magn Reson Med.* 2015;73:633-645. doi:10.1002/mrm.25179
- 35. Cao Z, Donahue MJ, Ma J, Grissom WA. Joint design of large-tip-angle parallel RF pulses and blipped gradient trajectories. *Magn Reson Med.* 2016;75:1198-1208. doi:10.1002/mrm.25739
- 36. Frank M, Wolfe P. An algorithm for quadratic programming. *Nav Res Logist Q.* 1956;3:95-110.
- Funai AK, Fessler JA, Yeo DTB, Olafsson VT, Noll DC. Regularized field map estimation in MRI. *IEEE Trans Med Imaging*. 2008;27:1484-1494. doi:10.1109/TMI.2008.923956
- 38. Chung S, Kim D, Breton E, Axel L. Rapid B_1^+ mapping using a preconditioning RF pulse with TurboFLASH readout. *Magn Reson Med.* 2010;64:439-446. doi:10.1002/mrm.22423
- 39. Layton KJ, Kroboth S, Jia F, et al. Pulseq: a rapid and hardware-independent pulse sequence prototyping framework: rapid hardware-independent pulse sequence prototyping. *Magn Reson Med.* 2017;77:1544-1552. doi:10.1002/mrm.26235
- Uecker M, Lai P, Murphy MJ, et al. ESPIRiT—an eigenvalue approach to autocalibrating parallel MRI: where SENSE meets GRAPPA. Magn Reson Med. 2014;71:990-1001. doi:10.1002/mrm.24751
- 41. Pruessmann KP, Weiger M, Scheidegger MB, Boesiger P. SENSE: sensitivity encoding for fast MRI. *Magn Reson Med*. 1999;42:952-962. doi:10.1002/(SICI)1522-2594(199911)42:5 <952::AID-MRM16>3.0.CO;2-S
- Malik SJ, Keihaninejad S, Hammers A, Hajnal JV. Tailored excitation in 3D with spiral nonselective (SPINS) RF pulses. *Magn Reson Med.* 2012;67:1303-1315. doi:10.1002/mrm.23118
- Setsompop K, Wald LL, Alagappan V, Gagoski BA, Adalsteinsson E. Magnitude least squares optimization for parallel radio frequency excitation design demonstrated at 7 Tesla with eight channels. *Magn Reson Med.* 2008;59:908-915. doi:10.1002/mrm.21513
- 44. Pfeuffer J, Van De Moortele PF, Yacoub E, et al. Zoomed functional imaging in the human brain at 7 Tesla with simultaneous high spatial and high temporal resolution. *Neuroimage*. 2002;17:272-286. doi:10.1006/nimg.2002.1103
- 45. Eberhardt B, Poser BA, Shah NJ, Felder J. Application of evolution strategies to the design of SAR efficient parallel transmit multi-spoke pulses for ultra-high field MRI. *IEEE Trans Med Imaging*. 2020;39:4225-4236. doi:10.1109/TMI.2020.3013982
- 46. Martin JB, Sappo CR, Hardy BM, Grissom WA. A minibatch alternating projections algorithm for robust and efficient magnitude least-squares RF pulse design in MRI. *IEEE Trans Med Imaging*. 2025;44:1556-1567. doi:10.1109/TMI.2024.3515035
- 47. Gras V, Mauconduit F, Vignaud A, et al. Design of universal parallel-transmit refocusing $k_{\rm T}$ -point pulses and application to 3D T $_2$ -weighted imaging at 7T. Magn Reson Med. 2018;80:53-65. doi:10.1002/mrm.27001
- Nocedal J, Wright SJ. Numerical Optimization., New York, USA: Springer; 1999.

- 49. Li B, Coutino M, Giannakis BG, Leus G. A momentum-guided Frank-Wolfe algorithm. *IEEE Trans Signal Process*. 2021;69:3597-3611. doi:10.1109/TSP.2021.3087910
- Gras V, Vignaud A, Amadon A, Le Bihan D, Boulant N. Universal pulses: a new concept for calibration-free parallel transmission. *Magn Reson Med.* 2017;77:635-643. doi:10.1002/mrm.26148
- Van Damme L, Mauconduit F, Chambrion T, Boulant N, Gras V.
 Universal nonselective excitation and refocusing pulses with improved robustness to off-resonance for magnetic resonance imaging at 7 Tesla with parallel transmission. *Magn Reson Med.* 2021;85:678-693. doi:10.1002/mrm.28441
- Yang J, Fajardo JE, Fessler JA, Gulani V, Nielsen JF, Jiang Y. Calibration-free multidimensional universal refocusing pulse design for 3D reduced field-of-view prostate imaging. *Proceedings of the Annual Meeting of ISMRM*; 2024:4094.

SUPPORTING INFORMATION

Additional supporting information may be found in the online version of the article at the publisher's website.

Figure S1. (A) B_0 map of phantom. (B) B_1^+ map of phantom. (C) Target region of interest (ROI) over which the radiofrequency (RF) pulse was designed to excite or refocus the magnetization. A transition was considered. The width of the transition band ("don't care" region) was equal to 20% of the ROI width. (D) Spatial weighting function used in the optimization.

Figure S2. (A,B) Magnitude and phase of radiofrequency (RF) waveforms of the small-tip angle pulse of 30°, scaled small-tip angle pulse for 90°, and optimized three-dimensional (3D) 90° excitation pulse. (C) Initial gradient waveform that is also the gradient waveform for the small-tip-angle pulses. (D) Optimized gradient waveform the 3D 90° excitation. (E) Excitation k-space of the initial gradients and optimized gradients. The optimized 3D excitation pulse has smaller peak RF than scaling the small-tip-angle pulse to 90°.

Figure S3. (A) Simulated $|M_{xy}|$ of the small-tip-angle 30° pulse. (B) Simulated $|M_{xy}|$ of the small-tip-angle pulse that was scaled to 90°. (C) Simulated $|M_{xy}|$ of the optimized 3D excitation pulse.

Figure S4. (A,B) Magnitude and phase of radiofrequency (RF) waveforms of the small-tip angle pulse of 30°, scaled small-tip-angle pulse for 180°, and optimized three-dimensional (3D) refocusing pulse. (C) Initial gradient waveform that is also the gradient waveform for the small-tip-angle pulses. (D) Optimized gradient waveform the 3D refocusing. (E) Excitation k-space of the initial gradients and optimized gradients. The optimized 3D refocusing pulse has smaller-peak RF than scaling the small-tip-angle pulse to 180°.

Figure S5. (A) Simulated refocusing profile of the small-tip-angle 30° pulse. (B) Simulated refocusing profile

of the small-tip-angle pulse that was scaled to 180°. (C) Simulated refocusing profile of the optimized three-dimensional (3D) refocusing pulse.

Figure S6. (A) Cost and root mean square error (RMSE) during the three-dimensional (3D) excitation optimization with gradient waveforms initialized by extend KT-points. (B) Cost and RMSE during the 3D refocusing optimization with gradient waveforms initialized by extended KT-points.

Figure S7. (A) Simulated excitation profiles at the center slice and root mean square error (RMSE) after different optimization time. (B) Simulated refocusing profiles at the center slice and RMSE after different optimization time.

Figure S8. Pulse initializations using extended KT-points trajectory. (A) Initial gradient using extended KT-points method. (B) Excitation k-space of the gradient waveform. (C,D) Magnitude and phase of radiofrequency (RF) waveforms that are randomly initialized and designed with 30° small-tip angle for target region of interest (ROI).

Figure S9. Pulse initializations using spiral nonselective (SPINS) trajectory. (A) Initial gradient using SPINS. (B) Excitation k-space of the gradient waveform. (C,D) Magnitude and phase of radiofrequency (RF) waveforms that are randomly initialized and designed with 30° small-tip angle for target region of interest (ROI).

Figure S10. Optimization of three-dimensional (3D) refocusing using different initializations. (A) Cost function. (B) Root mean square error (RMSE) evaluated in region of interest (ROI). (C) RMSE evaluated in outer volume (OV). **Figure S11**. Simulated refocusing profiles in $|\beta^2|$ that were optimized from different initializations: (1) extended KT-points trajectory and 30° small-tip-angle radiofrequency (RF) waveform; (2) extended KT-points trajectory and randomly initialized RF waveform; (3) spiral nonselective (SPINS) trajectory and 30° small-tip-angle RF waveform; and (4) SPINS trajectory and randomly initialized RF waveform.

Figure S12. Optimization of three-dimensional (3D) refocusing using extended KT-points trajectory and spiral nonselective (SPINS) trajectory with two optimization strategies: (1) optimizing both radiofrequency (RF) and gradient waveforms; and (2) only optimizing RF waveform. (A) Cost function. (B) Root mean square error (RMSE) evaluated in region of interest (ROI). (c) RMSE evaluated in outer volume (OV). The initial RF waveform is designed for 30° small-tip excitation.

Figure S13. Simulated refocusing profiles $|\beta^2|$ of pulse optimized using two different strategies: (1) optimizing both radiofrequency (RF) and gradient waveforms; and (2) only optimizing RF waveform.

Figure S14. Optimized waveforms of three-dimensional (3D) refocusing pulse with spiral nonselective (SPINS)

trajectory as the initialization. (A) Three-dimensional (3D) refocusing pulse obtained by optimizing both radiofrequency (RF) and gradient waveforms. (B) Three-dimensional (3D) refocusing pulse obtained by optimizing only RF waveform. (C) Excitation k-space trajectory for gradients.

Figure S15. Optimized radiofrequency (RF) waveforms using different cost functions for the excitation pulse design.

Figure S16. The optimization using different cost functions for the excitation pulse design problem.

Figure S17. Simulated M_{xy} profiles of three-dimensional (3D) 90° excitation pulses optimized using Bloch simulator and spin-domain simulator.

Figure S18. Optimized three-dimensional (3D) 90° excitation pulses using spin-domain simulator and Bloch simulator.

Figure S19. Simulated refocusing profile (β^2) of 180° inversion pulse (optimized using Bloch simulator) and 180° refocusing pulse (optimized using spin-domain simulator). A pair of red arrows compares the phase of β^2 within the region of interest (ROI). The phase of optimized refocusing pulse is more uniform.

Figure S20. The 180° refocusing pulse optimized using spin-domain simulator and the 180° inversion pulse optimized using Bloch simulator.

Table S1. Sequences and parameters for in vivo experiments. All the experiments acquired images of 32 slices with slice thickness = 3 mm.

How to cite this article: Yang J, Nielsen J-F, Fessler JA, Jiang Y. Multidimensional RF pulse design using auto-differentiable spin-domain optimization and its application to reduced field-of-view imaging. Magn Reson Med. 2025;94:1963-1981. doi: 10.1002/mrm.30607

Supporting Information

A. Explicit Jacobian of the spin domain representation

In our implementation, the real and imaginary parts of α_j and β_j were treated as four real numbers (i.e., $\alpha_j = \alpha_{j,re} + i\alpha_{j,im}$, and $\beta_j = \beta_{j,re} + i\beta_{j,im}$) where j denotes j-th time step during the simulation. A spin-domain rotation update step

$$\begin{bmatrix} \alpha_j \\ \beta_j \end{bmatrix} = \begin{bmatrix} a_j & -b_j^* \\ b_j & a_i^* \end{bmatrix} \begin{bmatrix} \alpha_{j-1} \\ \beta_{j-1} \end{bmatrix},$$

can then be written as the following equivalent expression:

$$\begin{bmatrix} \alpha_{j,re} \\ \alpha_{j,im} \\ \beta_{j,re} \\ \beta_{j,im} \end{bmatrix} = R_{ab}^{(j)} \begin{bmatrix} \alpha_{j-1,re} \\ \alpha_{j-1,im} \\ \beta_{j-1,re} \\ \beta_{j-1,im} \end{bmatrix},$$
 (S1)

where

$$R_{ab}^{(j)} = \begin{bmatrix} a_{j,re} & -a_{j,im} & -b_{j,re} & -b_{j,im} \\ a_{j,im} & a_{j,re} & b_{j,im} & -b_{j,re} \\ b_{j,re} & -b_{j,im} & a_{j,re} & a_{j,im} \\ b_{i,im} & b_{i,re} & -a_{i,im} & a_{i,re} \end{bmatrix}.$$
(S2)

This matrix $R_{ab}^{(j)}$ is also the Jacobian matrix for calculating derivatives:

$$\frac{\partial(\alpha_{j,re},\alpha_{j,im},\beta_{j,re},\beta_{j,im})}{\partial(\alpha_{j-1,re},\alpha_{j-1,im},\beta_{j-1,re},\beta_{j-1,im})} = R_{ab}^{(j)}$$
 (S3)

Similarly, the matrix

$$R_{\alpha\beta}^{(j-1)} = \begin{bmatrix} \alpha_{j-1,re} & -\alpha_{j-1,im} & -\beta_{j-1,re} & -\beta_{j-1,im} \\ \alpha_{j-1,im} & \alpha_{j-1,re} & -\beta_{j-1,im} & \beta_{j-1,re} \\ \beta_{j-1,re} & \beta_{j-1,im} & \alpha_{j-1,re} & -\alpha_{j-1,im} \\ \beta_{j-1,im} & -\beta_{j-1,re} & \alpha_{j-1,im} & \alpha_{j-1,re} \end{bmatrix}$$
(S4)

gives the Jacobian matrix for

$$\frac{\partial(\alpha_{j,re},\alpha_{j,im},\beta_{j,re},\beta_{j,im})}{\partial(\alpha_{j,re},\alpha_{j,im},b_{j,re},b_{j,im})} = R_{\alpha\beta}^{(j-1)}.$$
 (S5)

For convenience let $\partial(\alpha_j, \beta_j)/\partial(\alpha_{j-1}, \beta_{j-1})$ denote the Jacobian in Eq. S3 and let $\partial(\alpha_j, \beta_j)/\partial(\alpha_{j-1}, b_{j-1})$ denote the Jacobian in Eq. S5. Using these relationships, the Jacobian matrix for the

final state α_T , β_T with respect to a_t , b_t for all time points t can be iteratively computed by applying the chain rule. Other Jacobians such as $\partial \mathcal{L}/\partial(\alpha_T,\beta_T)$, $\partial(a_t,b_t)/\partial \mathbf{g}_t$, and $\partial(a_t,b_t)/\partial \mathbf{b}_t$ which require much less computation are obtained by the auto-differentiation framework in PyTorch. We use this scheme to obtain the partial derivatives $\nabla_{\mathbf{b}}\mathcal{L}$ and $\nabla_{\mathbf{g}}\mathcal{L}$ for a given pulse and loss function.

B. Algorithms for Optimizing RF and Gradient Waveforms

Algorithm 1 describes the pseudo-code for RF and gradient waveform optimization.

Algorithm 1 Alternating minimization of b and g

Require: Input \mathbf{b} , \mathbf{g} , number of iterations K

for k = 1, 2, ..., K do

Fix **g**, update **b** using Frank-Wolfe algorithm

Fix b, update g using modified gradient descent

End for

Return b and g

To update \mathbf{b} , we used the Frank-Wolfe algorithm to constrain \mathbf{b} to be below the maximum RF amplitude. The update of \mathbf{b} for every time point t is given by

$$\mathbf{v}_{t} = -b_{\text{max}} \cdot \frac{\left(\nabla_{\mathbf{b}_{\text{old}}}\mathcal{L}\right)_{t}}{\left\|\left(\nabla_{\mathbf{b}_{\text{old}}}\mathcal{L}\right)_{t}\right\|_{2}},$$

$$\mathbf{d}_{t} = \mathbf{v}_{t} - (\mathbf{b}_{\text{old}})_{t},$$

$$(\mathbf{b}_{\text{new}})_{t} = (\mathbf{b}_{\text{old}})_{t} + \mu \mathbf{d}_{t}, \quad 0 < \mu \le 1,$$
(S6)

where the step size μ is found by backtracking line search.

To update **g**, we used a modified gradient descent approach by constraining the step size to ensure the update remained feasible. Considering the update

$$\mathbf{g}_{\text{new}} = \mathbf{g}_{\text{old}} - \eta \nabla_{\mathbf{g}_{\text{old}}} \mathcal{L}, \tag{S7}$$

the slew rate of \boldsymbol{g}_{new} is given by

$$\mathbf{D}\mathbf{g}_{\text{new}} = \mathbf{D}\mathbf{g}_{\text{old}} - \eta \mathbf{D}\nabla_{\mathbf{g}_{\text{old}}} \mathcal{L}. \tag{S8}$$

We first found the maximum step size η_{max} that satisfies the maximum gradient amplitude and the maximum slew rate constraints for every time point t by solving

$$\begin{aligned} & \left\| (\mathbf{g}_{\text{old}})_{t} - \eta_{\text{max}} (\nabla_{\mathbf{g}_{\text{old}}} \mathcal{L})_{t} \right\|_{\infty} \leq g_{\text{max}}, \\ & \left\| (\mathbf{D}\mathbf{g}_{\text{old}})_{t} - \eta_{\text{max}} (\mathbf{D}\nabla_{\mathbf{g}_{\text{old}}} \mathcal{L})_{t} \right\|_{\infty} \leq s_{\text{max}}. \end{aligned} \tag{S9}$$

Then the final step size η was found using backtracking line search to ensure the descent condition is satisfied.

C. RF Pulse Optimization

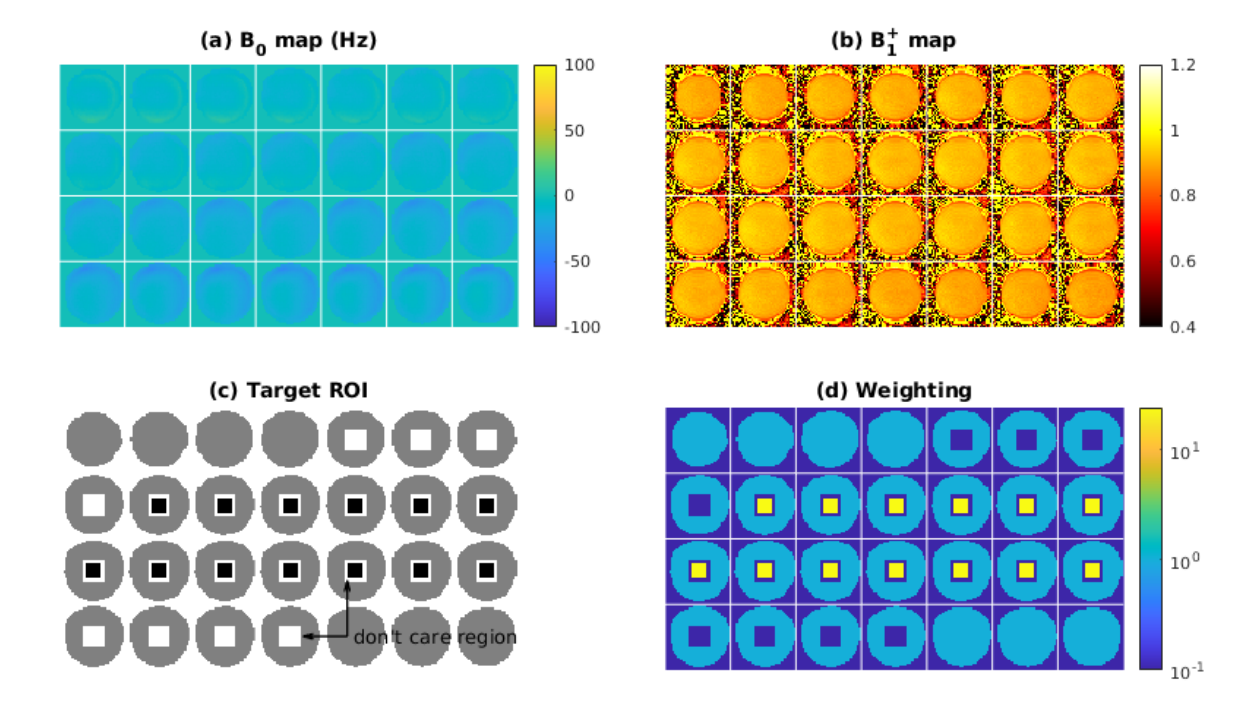


Figure S1. (a) B_0 map of phantom. (b) B_1^+ map of phantom. (c) Target ROI over which the RF pulse was designed to excite or refocus the magnetization. A transition was considered. The width of the transition band ("don't care" region) was equal to 20% of the ROI width. (d) Spatial weighting function used in the optimization.

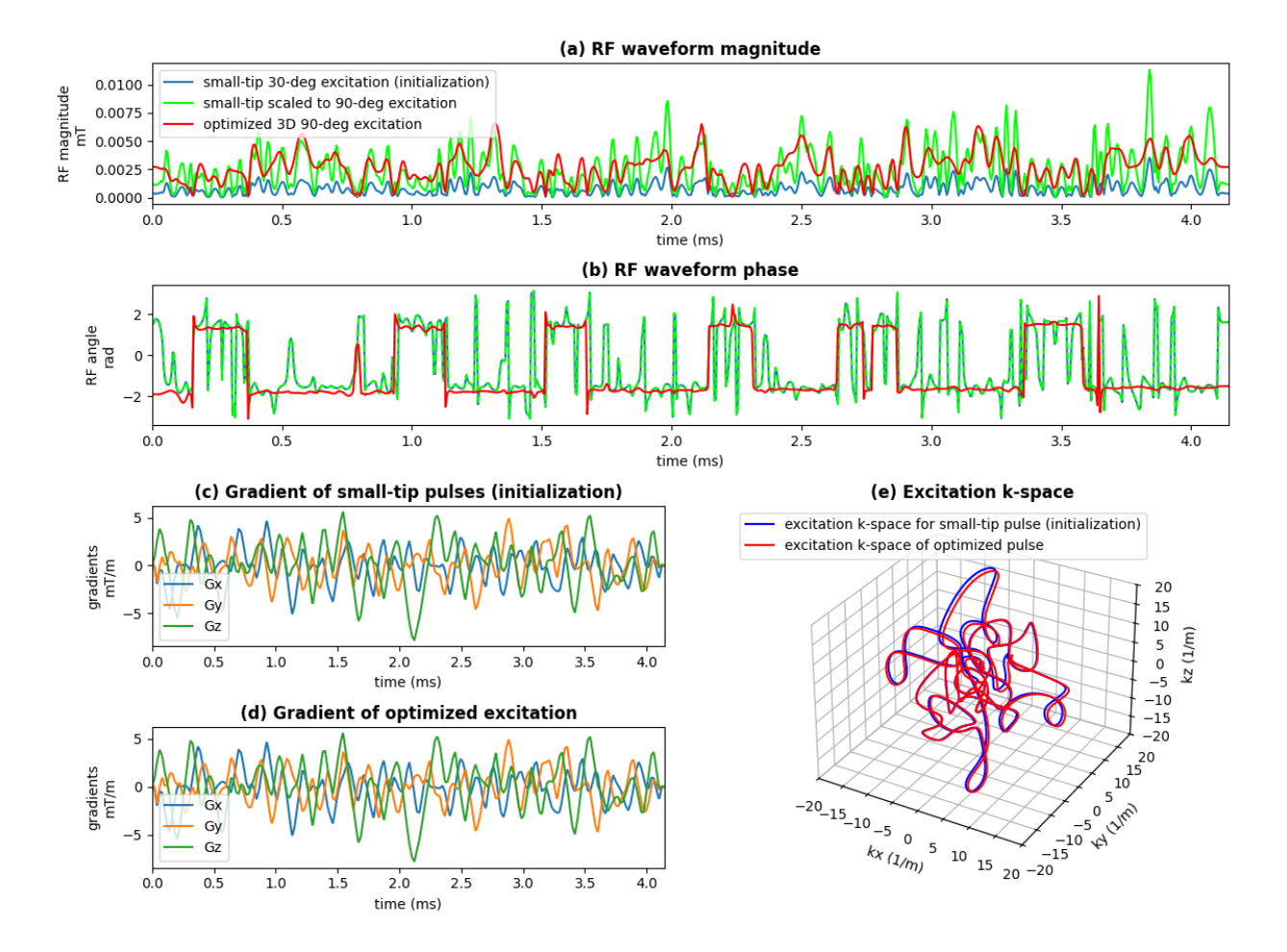


Figure S2. (a)(b) Magnitude and phase of RF waveforms of the small-tip angle pulse of 30°, scaled small-tip angle pulse for 90°, and optimized 3D 90° excitation pulse. (c) Initial gradient waveform which is also the gradient waveform for the small-tip angle pulses. (d) Optimized gradient waveform the 3D 90° excitation. (e) Excitation k-space of the initial gradients and optimized gradients. The optimized 3D excitation pulse has smaller peak RF than scaling the small-tip angle pulse to 90°.

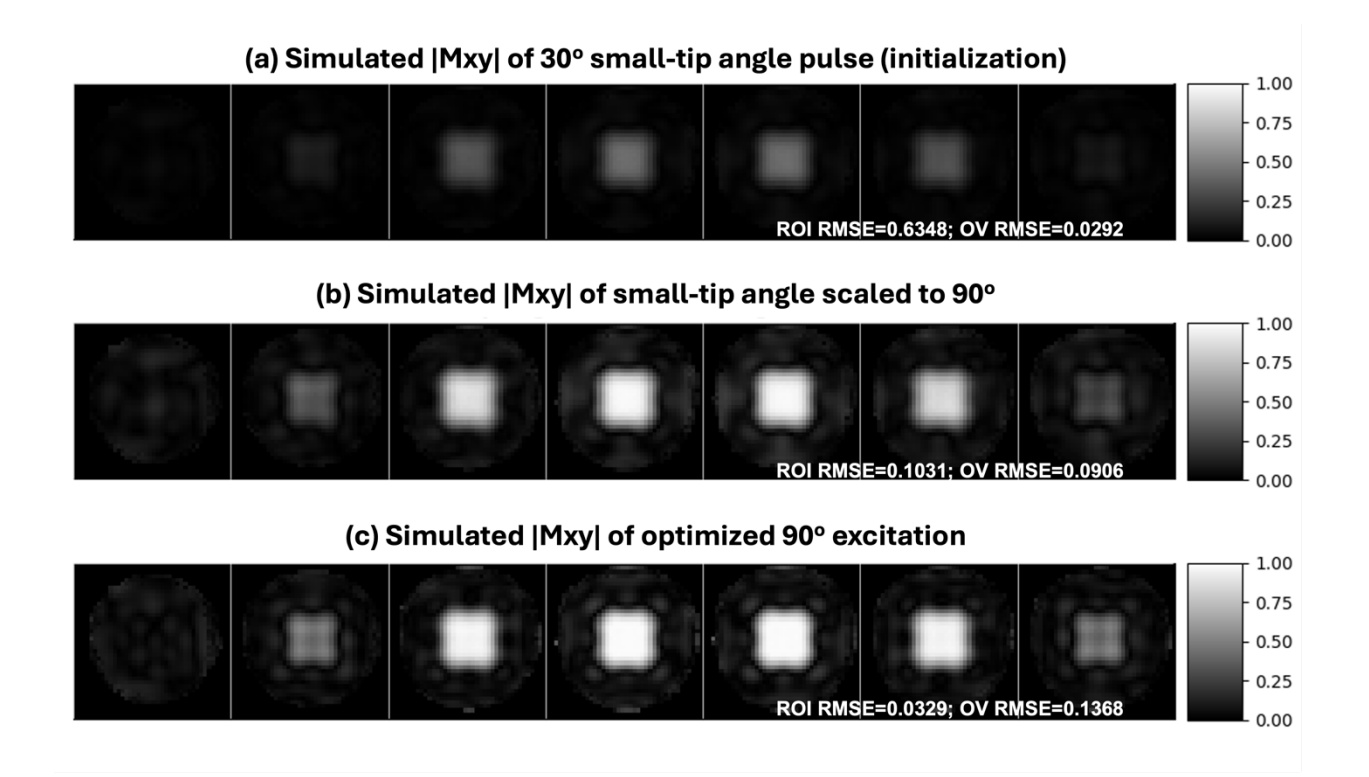


Figure S3. (a) Simulated $|M_{xy}|$ of the small-tip angle 30° pulse. (b) Simulated $|M_{xy}|$ of the small-tip angle pulse that was scaled to 90°. (c) Simulated $|M_{xy}|$ of the optimized 3D excitation pulse.

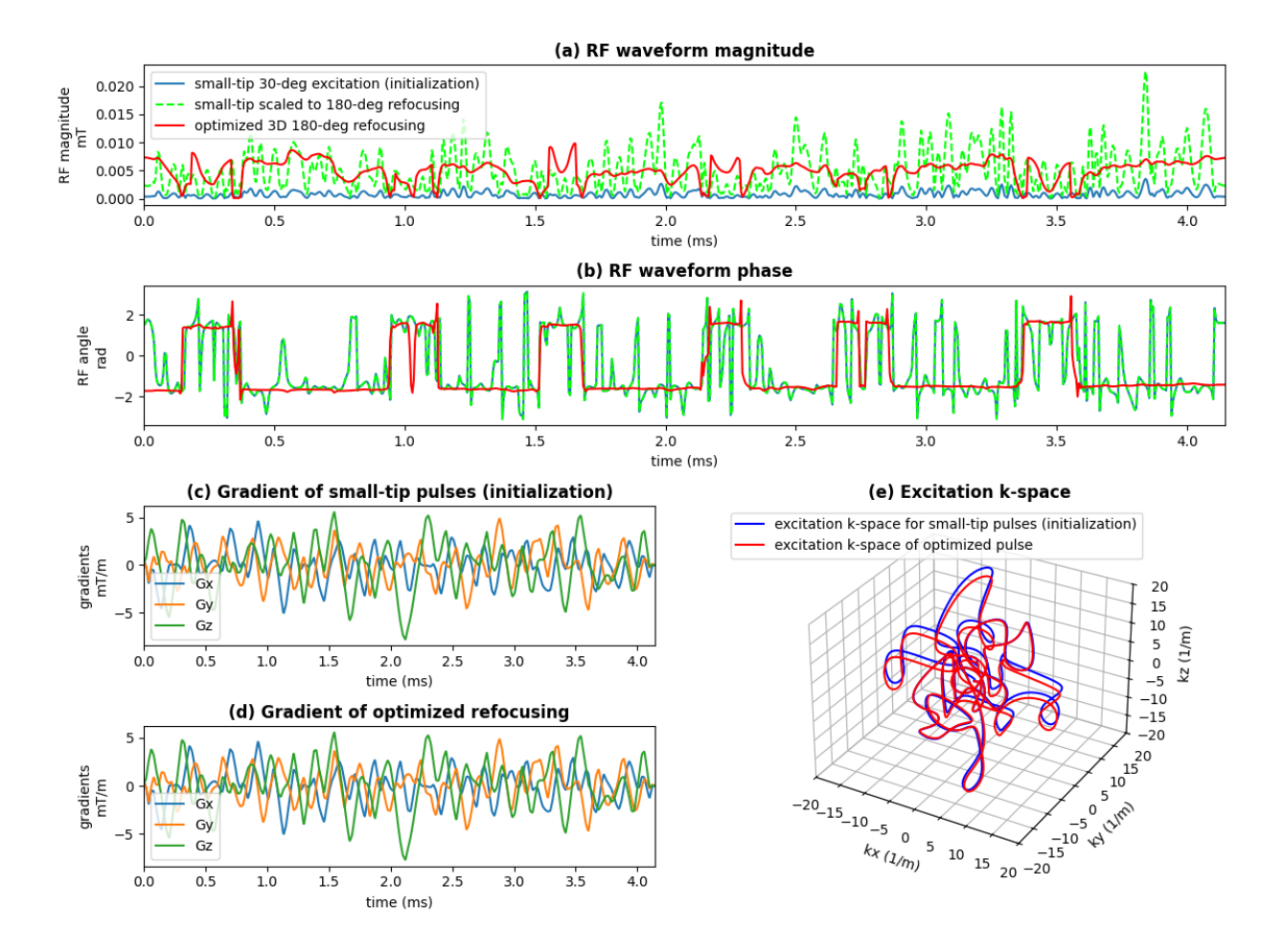


Figure S4. (a)(b) Magnitude and phase of RF waveforms of the small-tip angle pulse of 30°, scaled small-tip angle pulse for 180°, and optimized 3D refocusing pulse. (c) Initial gradient waveform which is also the gradient waveform for the small-tip angle pulses. (d) Optimized gradient waveform the 3D refocusing. (e) Excitation k-space of the initial gradients and optimized gradients. The optimized 3D refocusing pulse has smaller peak RF than scaling the small-tip angle pulse to 180°.

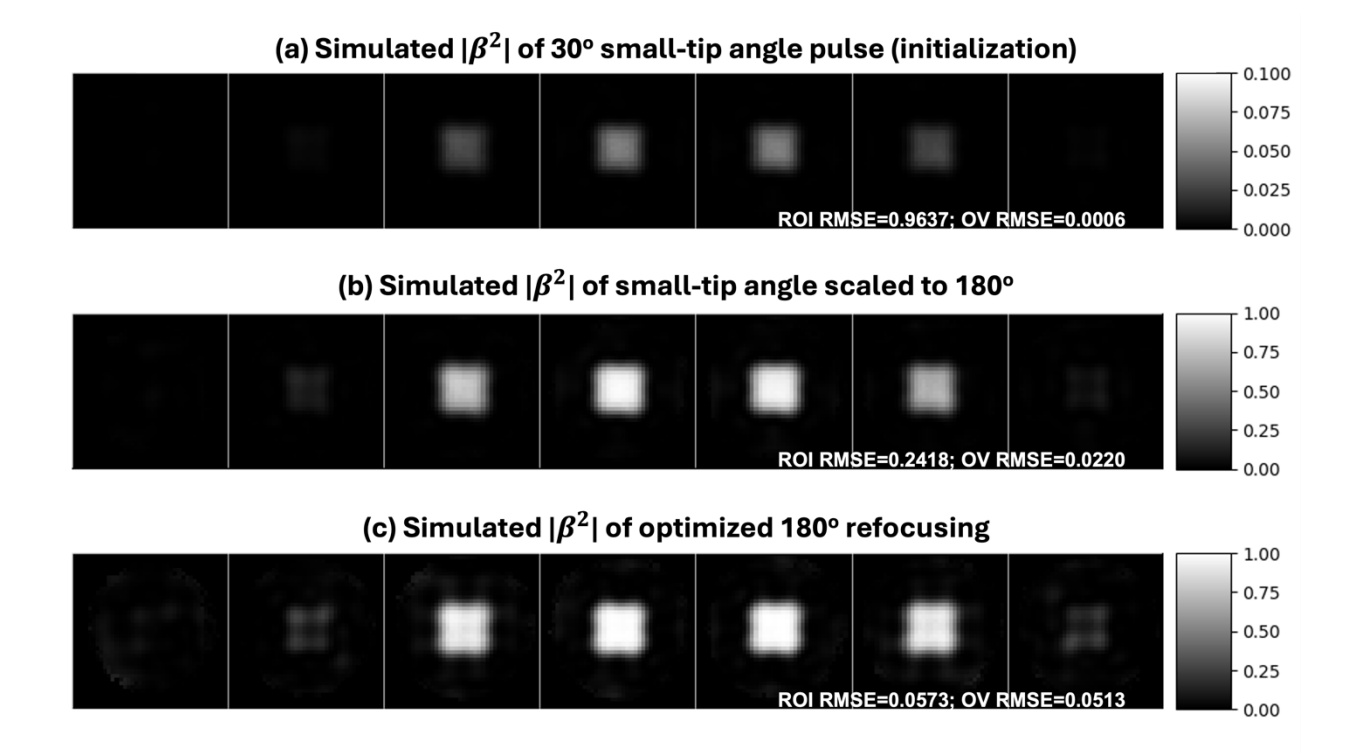


Figure S5. (a) Simulated refocusing profile of the small-tip angle 30° pulse. (b) Simulated refocusing profile of the small-tip angle pulse that was scaled to 180°. (c) Simulated refocusing profile of the optimized 3D refocusing pulse.

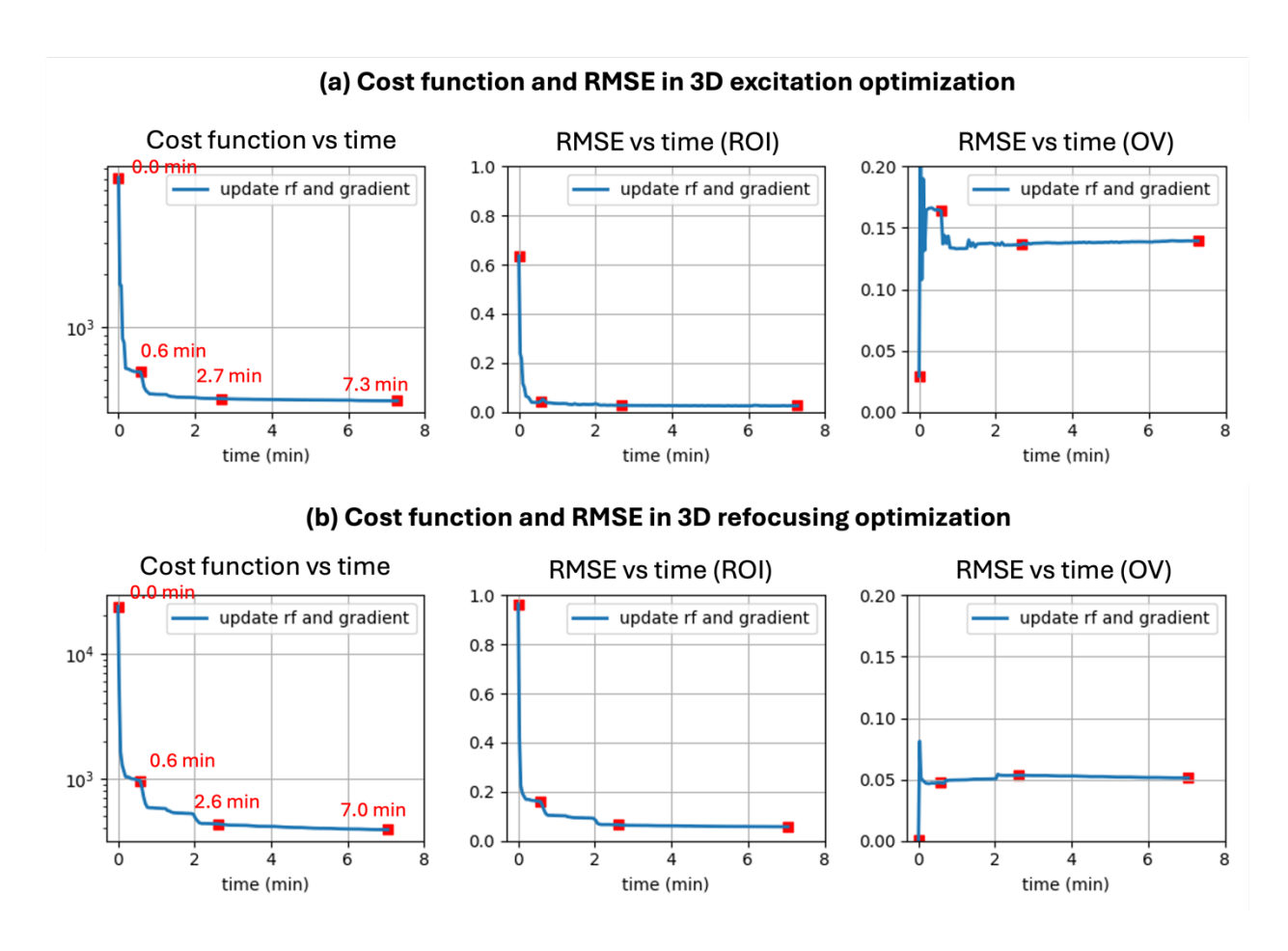


Figure S6. (a) Cost and RMSE during the 3D excitation optimization with gradient waveforms initialized by extend KT-points. (b) Cost and RMSE during the 3D refocusing optimization with gradient waveforms initialized by extended KT-points.

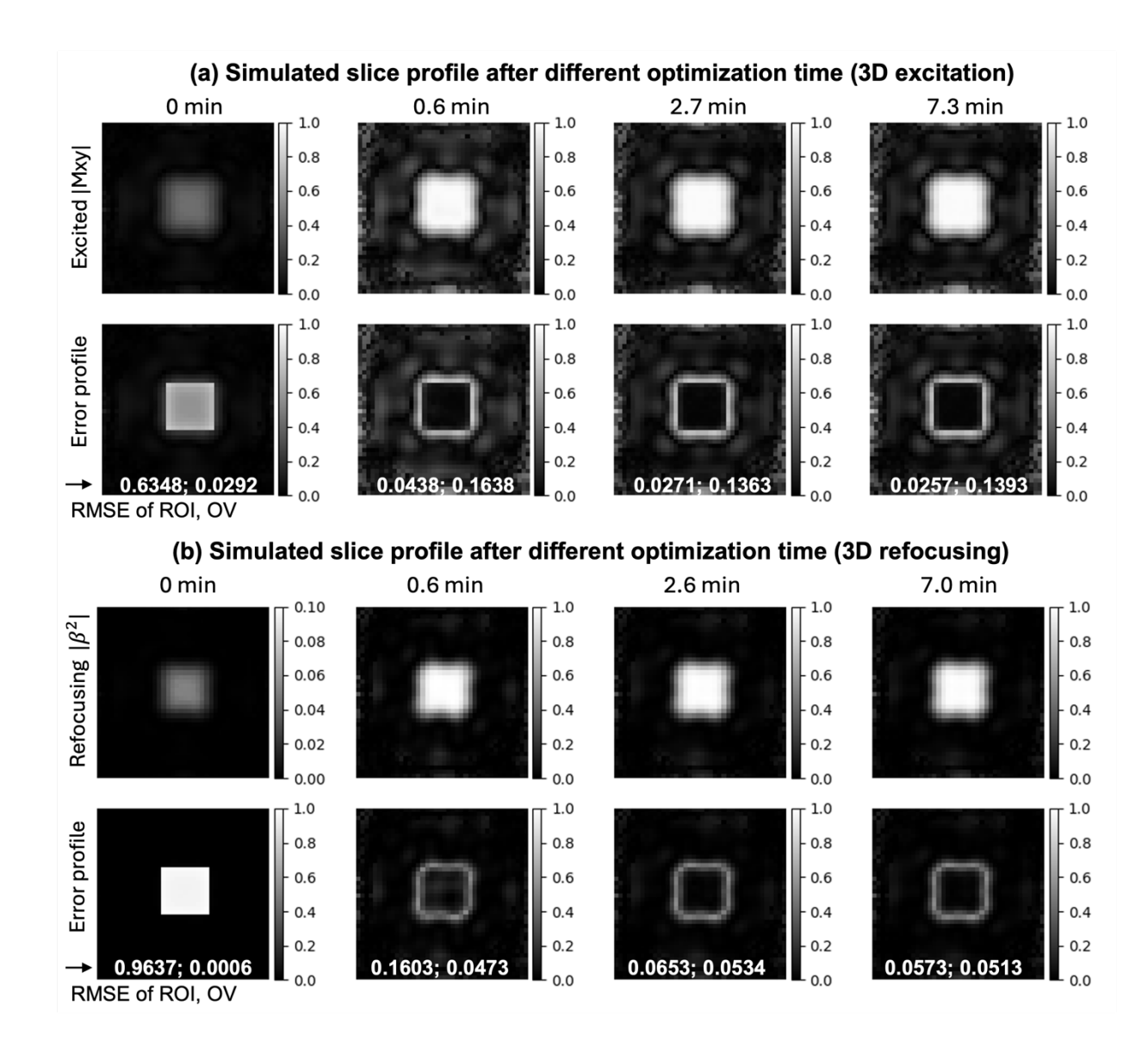


Figure S7. (a) Simulated excitation profiles at the center slice and RMSE after different optimization time. (b) Simulated refocusing profiles at the center slice and RMSE after different optimization time.

D. Effect of RF and Gradient Initializations

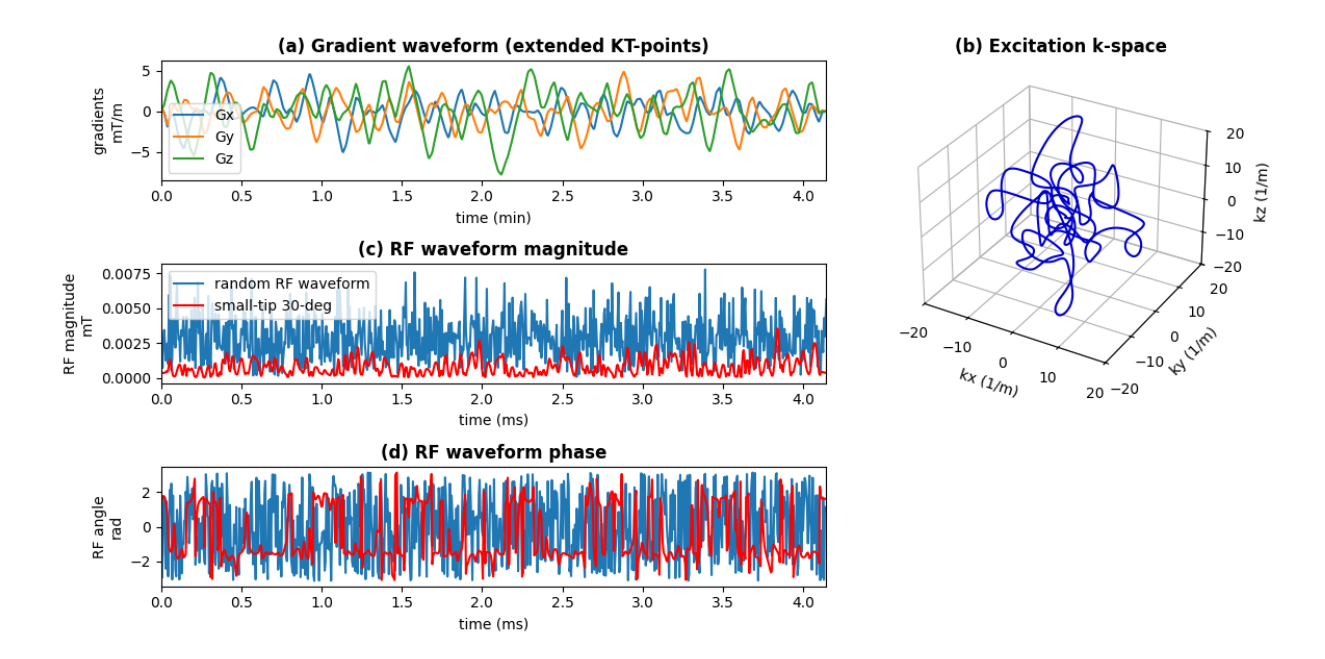


Figure S8. Pulse initializations using extended KT-points trajectory. (a) Initial gradient using extended KT-points method. (b) Excitation k-space of the gradient waveform. (c)(d) Magnitude and phase of RF waveforms that are randomly initialized and designed with 30° small-tip angle for target ROI.

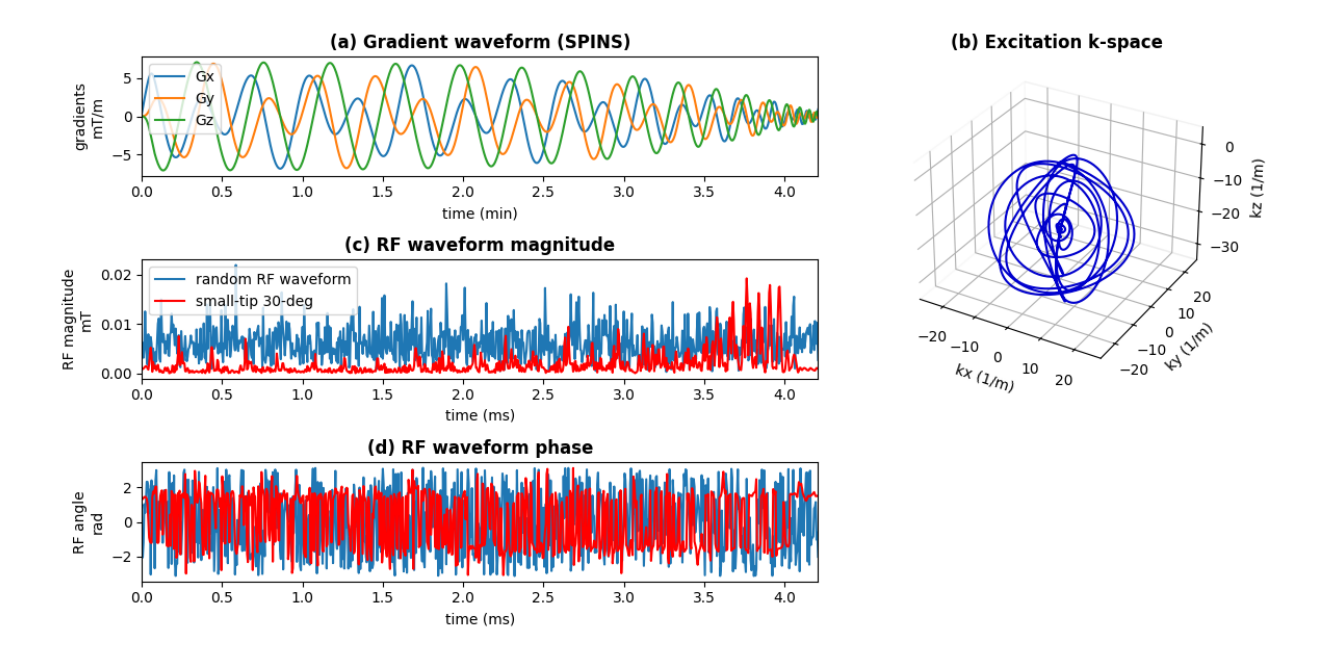


Figure S9. Pulse initializations using SPINS trajectory. (a) Initial gradient using SPINS. (b) Excitation k-space of the gradient waveform. (c)(d) Magnitude and phase of RF waveforms that are randomly initialized and designed with 30° small-tip angle for target ROI.

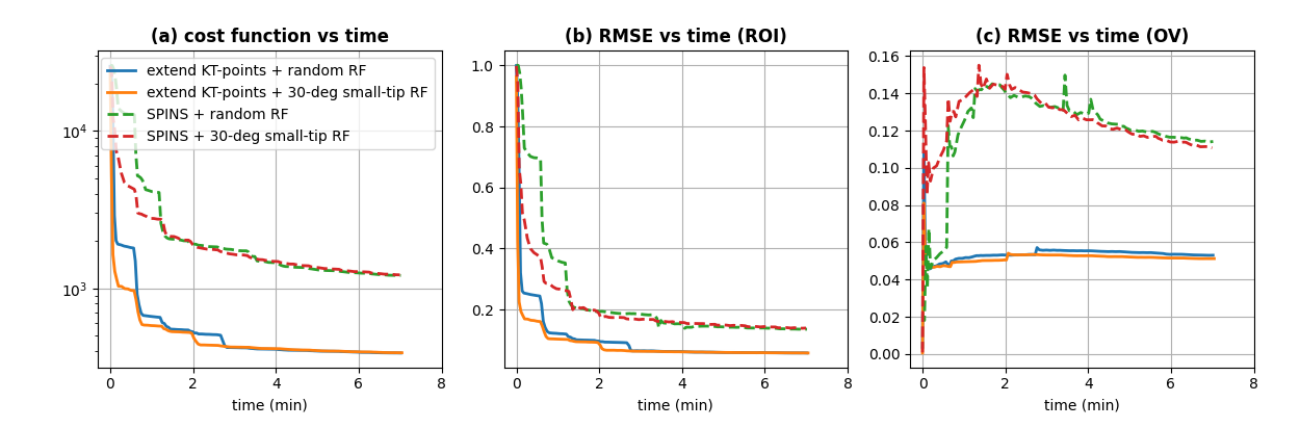


Figure S10. Optimization of 3D refocusing using different initializations. (a) Cost function. (b) RMSE evaluated in ROI. (c) RMSE evaluated in OV.

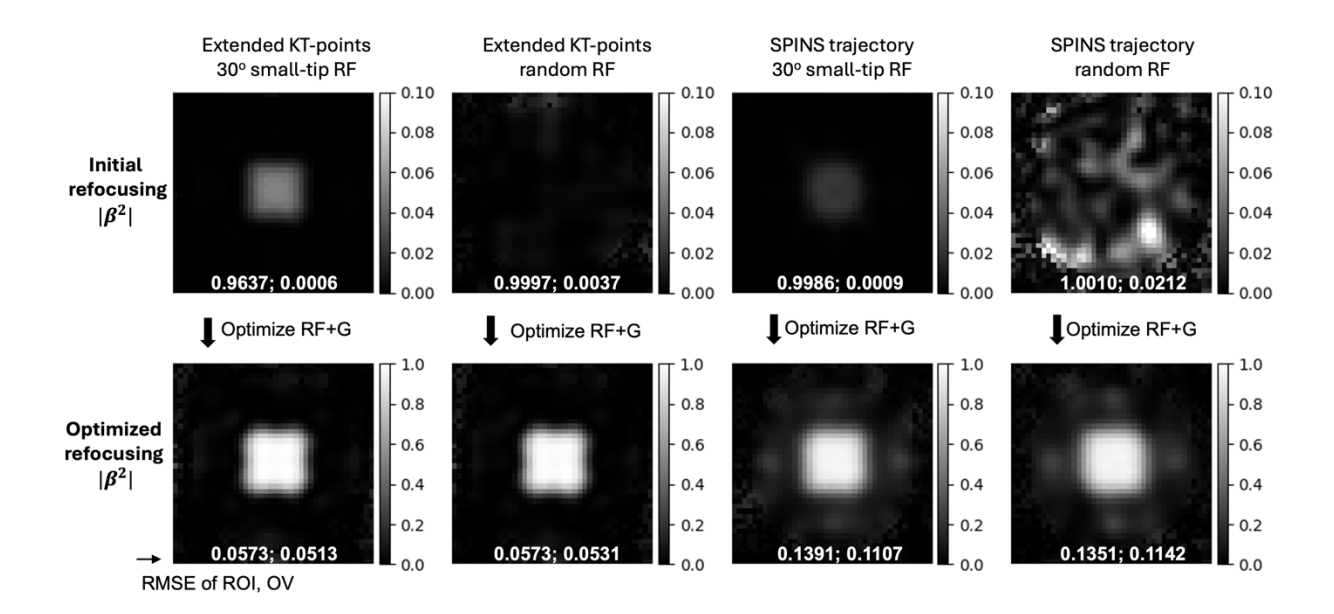


Figure S11. Simulated refocusing profiles in $|\beta^2|$ that were optimized from different initializations: 1) extended KT-points trajectory and 30° small-tip angle RF waveform; 2) extended KT-points trajectory and randomly initialized RF waveform; 3) SPINS trajectory and 30° small-tip angle RF waveform; 4) SPINS trajectory and randomly initialized RF waveform.

E. Effect of Gradient Updates During the Optimization

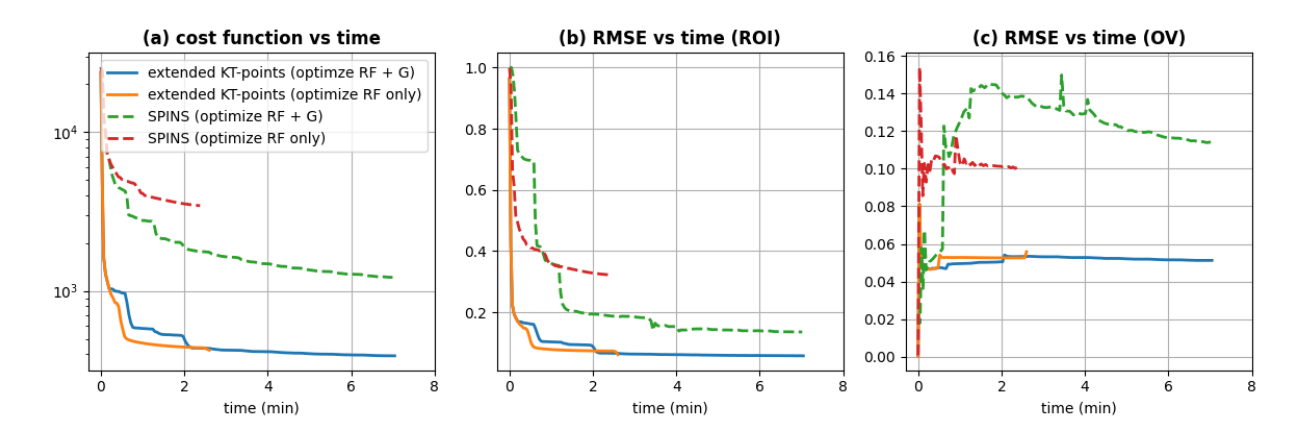


Figure S12. Optimization of 3D refocusing using extended KT-points trajectory and SPINS trajectory with two optimization strategies: 1) optimizing both RF and gradient waveforms; 2) only optimizing RF waveform. (a) Cost function. (b) RMSE evaluated in ROI. (c) RMSE evaluated in OV. The initial RF waveform is designed for 30° small-tip excitation.

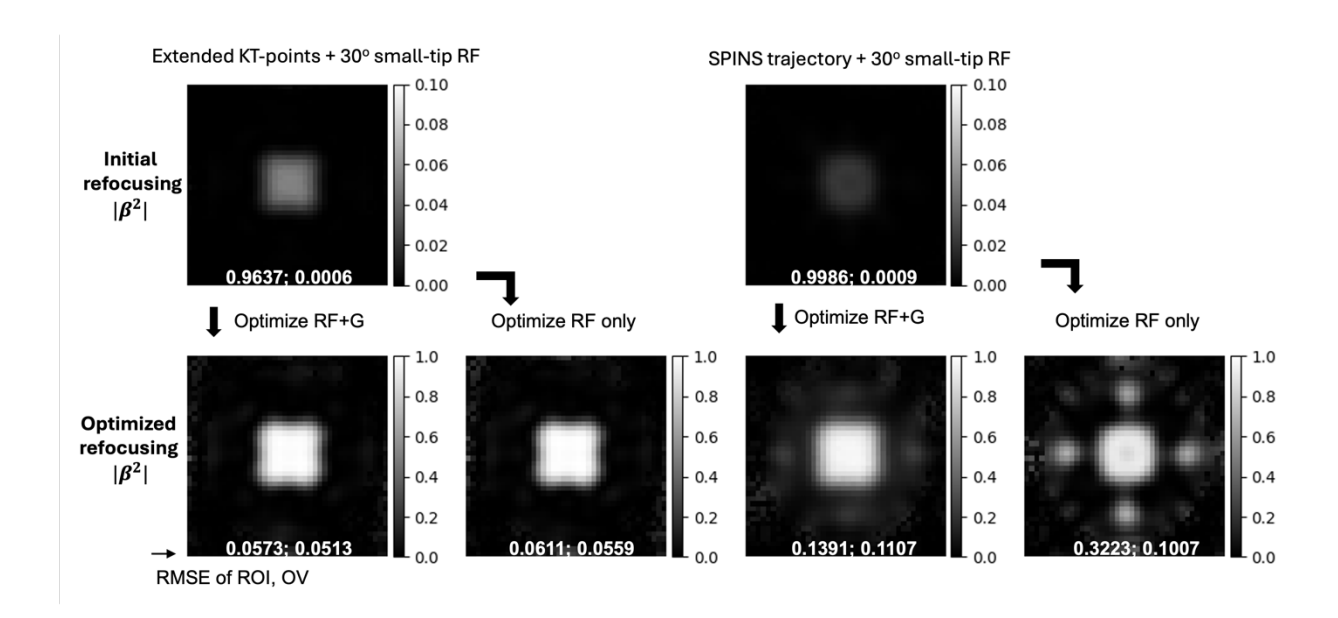


Figure S13. Simulated refocusing profiles $|\beta^2|$ of pulse optimized using two different strategies: 1) optimizing both RF and gradient waveforms; 2) only optimizing RF waveform.

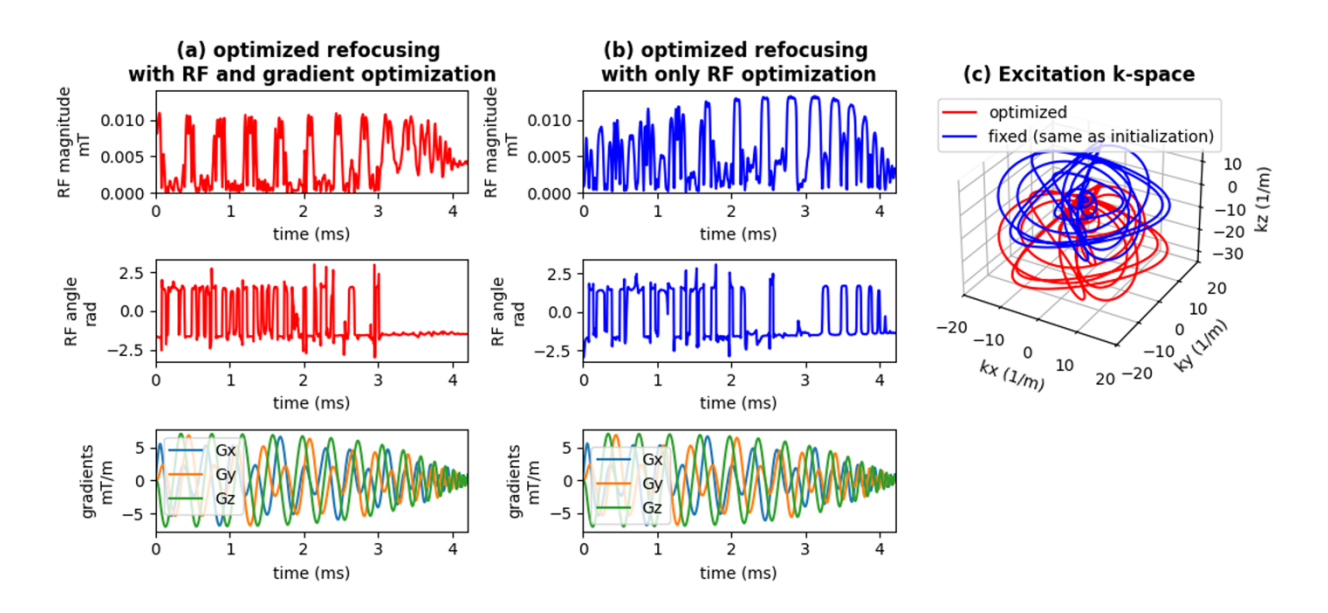


Figure S14. Optimized waveforms of 3D refocusing pulse with SPINS trajectory as the initialization. (a) 3D refocusing pulse obtained by optimizing both RF and gradient waveforms. (b) 3D refocusing pulse obtained by optimizing only RF waveform. (c) Excitation k-space trajectory for gradients.

F. Effect of Cost Functions on Excitation Optimization

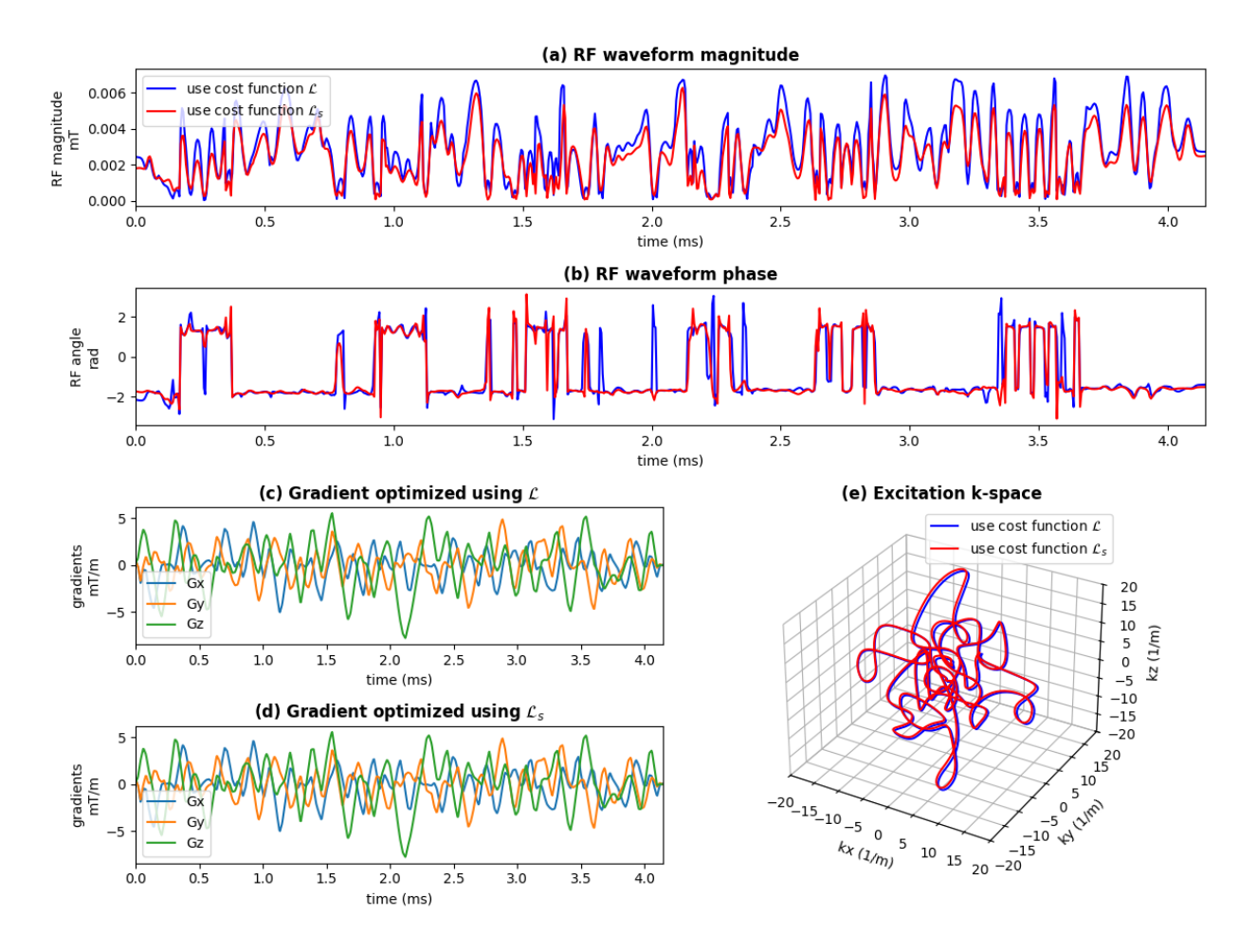


Figure S15. Optimized RF waveforms using different cost functions for the excitation pulse design.

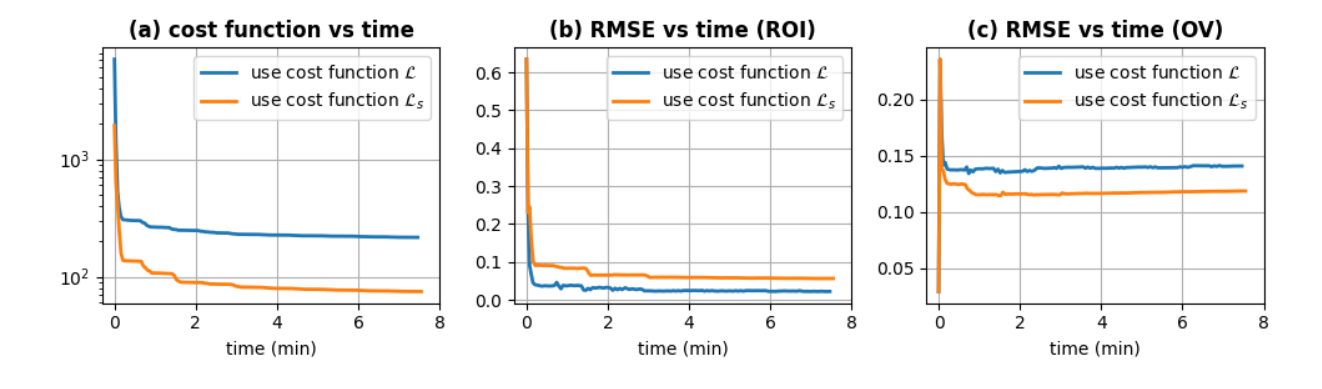


Figure S16. The optimization using different cost functions for the excitation pulse design problem.

G. Comparison with Other Design Methods

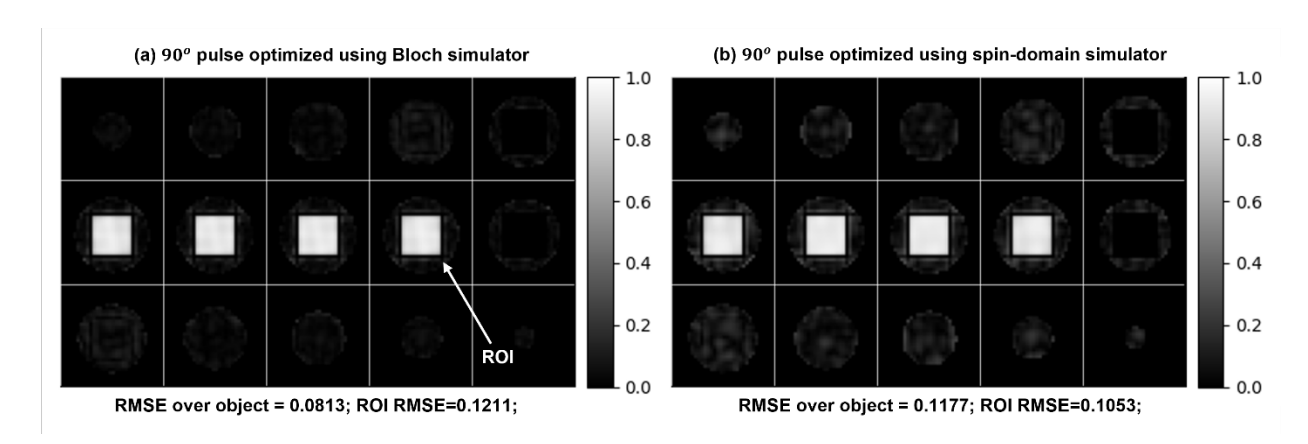


Figure S17. Simulated M_{xy} profiles of 3D 90° excitation pulses optimized using Bloch simulator and spin-domain simulator.

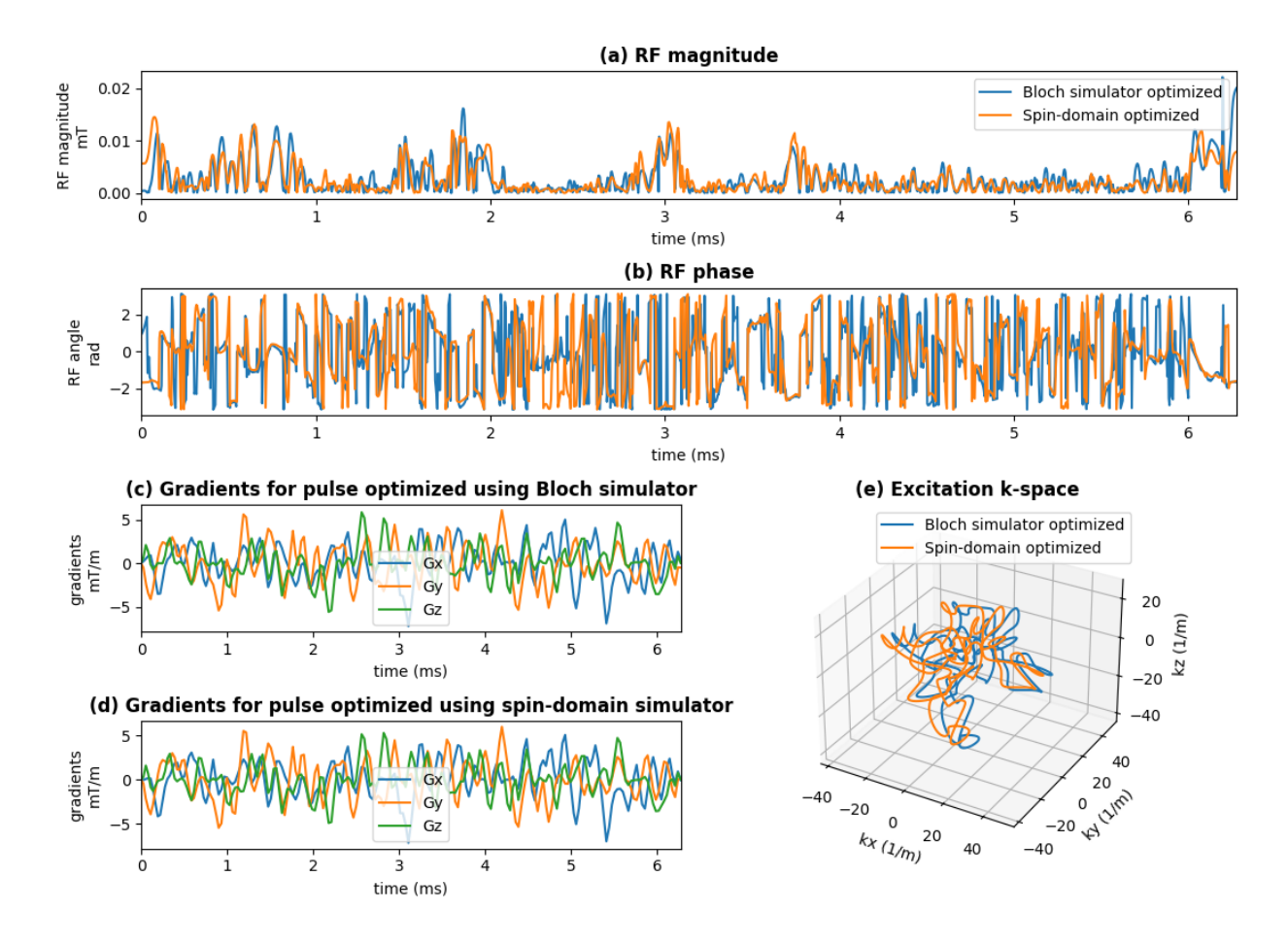


Figure S18. Optimized 3D 90° excitation pulses using spin-domain simulator and Bloch simulator.

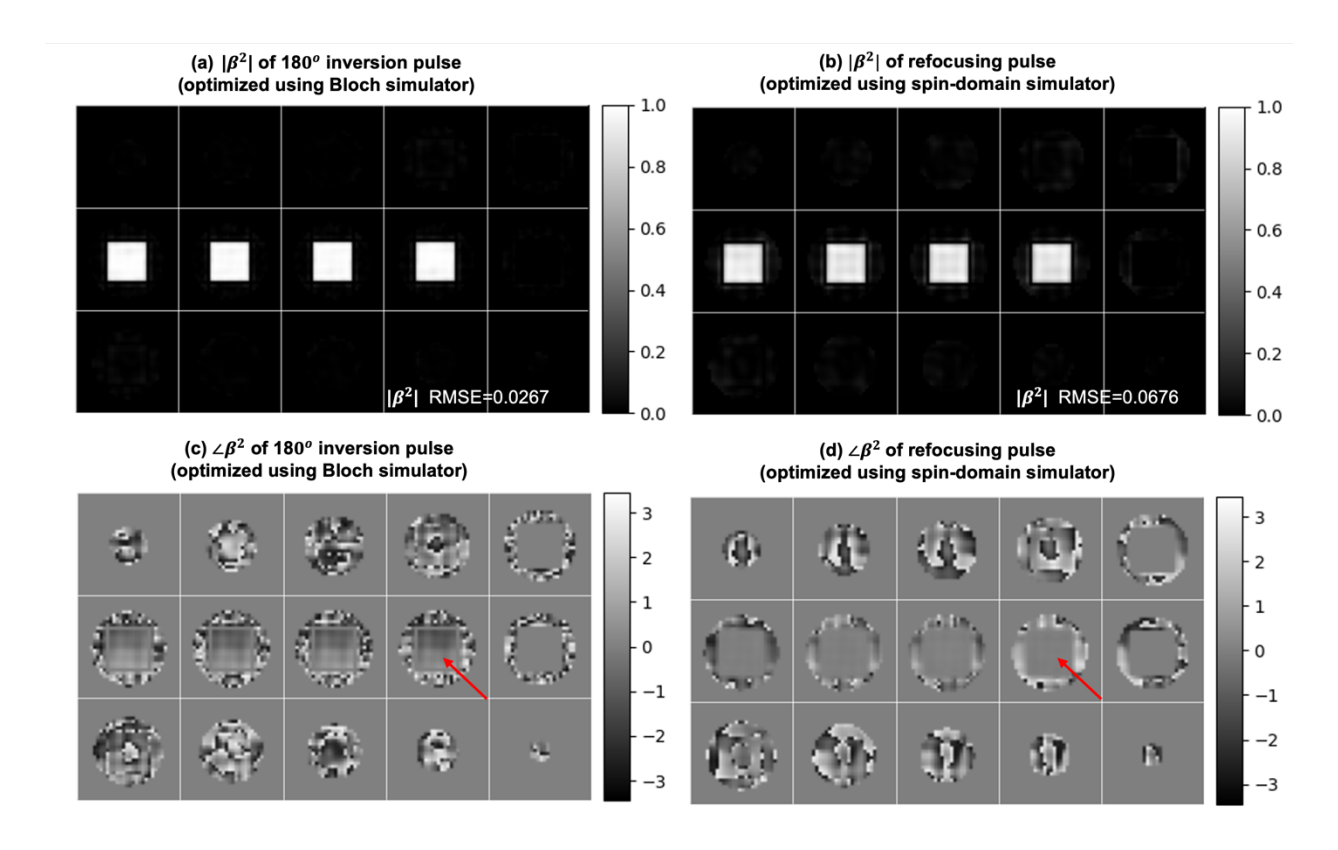


Figure S19. Simulated refocusing profile (β^2) of 180° inversion pulse (optimized using Bloch simulator) and 180° refocusing pulse (optimized using spin-domain simulator). A pair of red arrows compares the phase of β^2 within the ROI. The phase of optimized refocusing pulse is more uniform.

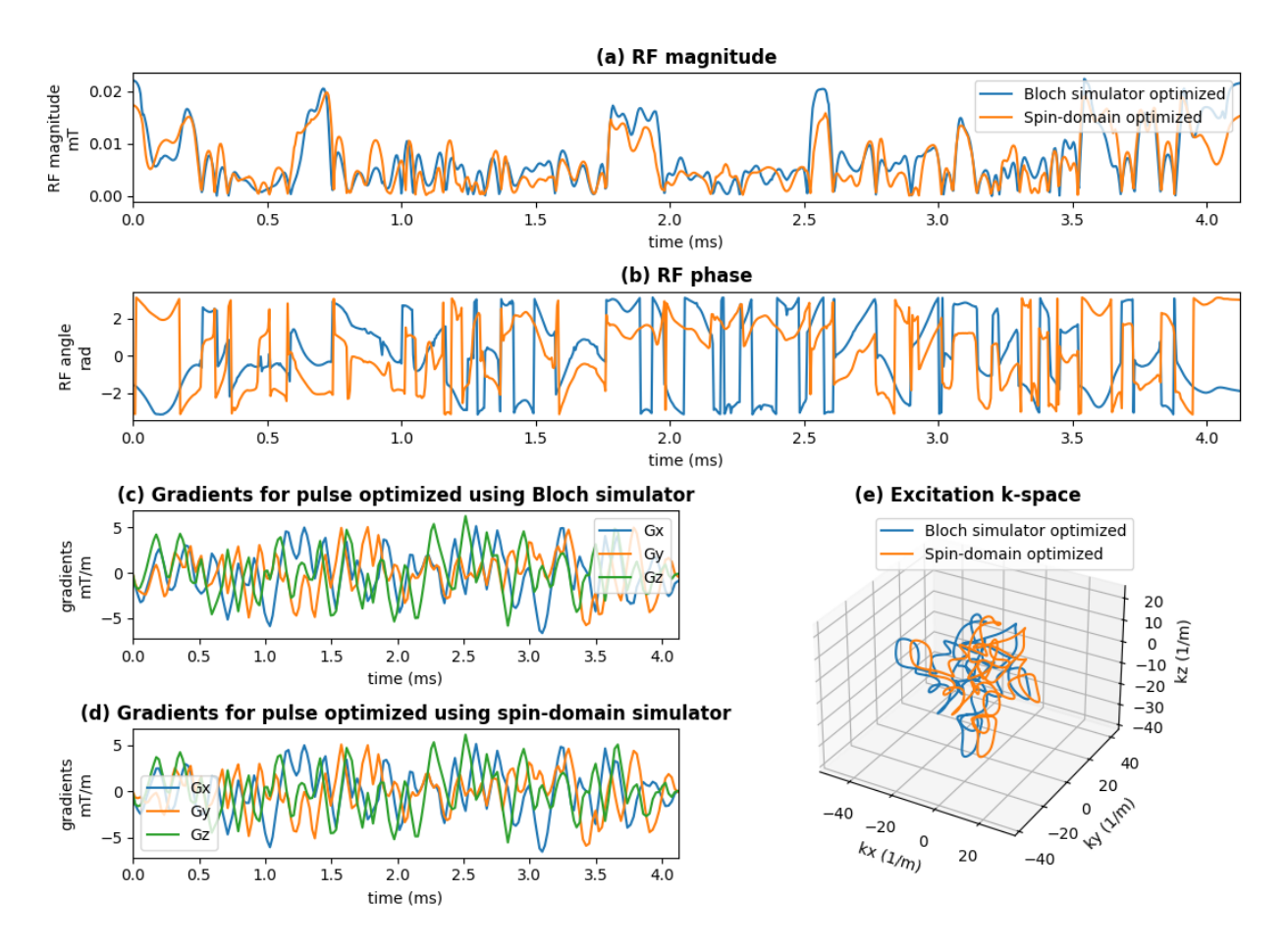


Figure S20. 180° refocusing pulse optimized using spin-domain simulator and 180° inversion pulse optimized using Bloch simulator.

H. Table of experiment sequence parameters for in vivo experiments

Table S1. Sequences and parameters for in vivo experiments. All the experiments acquired images of 32 slices with slice thickness = 3mm.

Experiment Sequence	Sequence	Excitation	Refocusing	FOV (mm²)	In-Plane Resolution (mm²)	EPI Phase Encoding	TR/TE (ms/ms)	Acquisition Size	Average	Scan Time (s)
Brain	3D SE	1D 90°	1D 180°	256×256	2×2	75% Partial	1000/64	128×128×32	1	32
	3D SE	3D 90°	1D 180°	256×256	2×2	Fourier and R=2 acceleration	1000/64	128×128×32	_	32
	3D SE	1D 90°	3D 180°	256×256	2×2		1000/64	128×128×32	_	32
	3D SE	3D 90°	3D 180°	256×256	2×2		1000/64	128×128×32	_	32
	3D SE	3D 90°	3D 180°	128×128	<u>*</u>		1000/64	128×128×32	—	32
	TSE	Slice 90o	Slice 180°	300×300	1×1	Turbo Factor=7	4000/62	304×308×32	-	70
Prostate	3D SE	1D 90°	1D 180°	384×384	3×3	75% Partial	1000/64	128×128×32	2	64
	3D SE	3D 90°	1D 180°	384×384	3×3	Fourier and R=2 acceleration	1000/64	128×128×32	7	64
	3D SE	1D 90°	3D 180°	384×384	3×3		1000/64	128×128×32	7	64
	3D SE	3D 90°	3D 180°	384×384	3×3		1000/64	128×128×32	7	64
	3D SE	3D 90°	3D 180°	128×128	<u>*</u>		1000/64	128×128×32	2	64
	TSE	Slice 90°	Slice 180°	384×384	1×1	Turbo Factor=7	3450/62	385×384×32	1	92